In-situ hierarchical micro/nanocrystals on copper substrate for enhanced boiling performance: an experimental study

Xiao Yuan[1], Yanping Du[1,2,*], Ruijie Yang[1], Guochao Fei[1], Chao Wang[3], Qian Xu[4], Chuan Li[5]

[1]China-UK Low Carbon College, Shanghai Jiao Tong University, Shanghai, 201306, China

[2] Department of Engineering, Faculty of Environment, Science and Economy, University of Exeter, Penryn Campus, Penryn, Cornwall TR109FE, UK

[3] Guangdong Provincial Key Laboratory on Functional Soft Condensed Matter, School of Materials and Energy, Guangdong University of Technology, Guangzhou 510006, China

[4] School of Energy and Environmental Engineering, Shunde Graduate School, University of Science and Technology Beijing, Beijing, 100083, China

[5] MOE Key Laboratory of Enhanced Heat Transfer and Energy Conservation, Beijing Key Laboratory of Heat Transfer and Energy Conversion, Beijing University of Technology, Beijing, 100124, China

* Correspondence: yanping.du@sjtu.edu.cn

Abstract: Micro/nano structures on the Cu substrate are normally used for the enhancing the heat transfer capacity for many boiling-related applications. Conventional methods for fabricating these structures, however, require additional processing equipment and involve relatively complex processes. In this study, a simple immersion method for generating in-situ micro/nanocrystal structures on Cu substrates is developed for simplifying the fabrication with reduced cost and improving the boiling performance in the meantime. Using characterization analytical instruments including SEM, AFM, XRD, EDS and XPS, the surface morphology and chemical contents of the micro- and nanocrystals generated on the Cu substrate were examined. The experimental results showed that the hierarchical micro/nanocrystals enabled simultaneous enhancements in critical heat flux (CHF) and heat transfer coefficient (HTC), indicating the superiority of the hierarchical micro/nanocrystals in facilitating the boiling performance compared to conventional structured surfaces. It is found that the nanosheet and micro-flowers (NSMF) surface provides the largest enhancement amongst other micro/ nano structures including the nanograss forests (NG), nanograss forests and micro-petals (NGMP), and nanograss forests and micro-flowers (NGMF). Comparatively, the CHF and HTC could achieve 65.7 W/cm^2 and 4.9 W/cm^{2}K, showing an increase of the CHF and HTC by 56.5 % and 170 %, respectively, using the smooth

surface in the same condition as the benchmark. It is implied that the liquid circulation is apparently promoted through the separation of vapor-liquid pathway and the bubble blanket formation is remarkably inhibited due to the special structure and morphology of the hierarchical surface. However, vital factors including the surface wettability and the experimental accuracy need to be considered for optimizing the boiling performance in diverse scenarios.

Key words: Immersion method; In-situ micro/nanocrystals; Hierarchical structure; liquid circulation; CHF

1. Introduction

Due to the significant latent heat associated with the working fluid's liquid-to-vapor phase change, nucleate boiling heat transfer has been used in many high energy-consuming applications, including electronic devices, nuclear reactors, lasers, and more [1-3]. In this phenomenon, heat transfer coefficient (HTC), which represents the ratio of heat flux to the wall superheat temperature, is used to show the heat removal capacity of the device. While the critical heat flux (CHF), is regarded as the terminal safety thread, which indicates a transient increase in surface temperature (approximately 1000 ℃) at this moment, causing severe damages to devices. Advanced boiling techniques that aim to concurrently improve the HTC and CHF must be developed in order to prevent safety issues like burnout and dry out for increasing the limit of heat transfer.

Previous research has demonstrated that the surface wettability and structure have a considerable impact on the onset of nucleate boiling (ONB), bubble growth and departure, as well as the CHF [4-8]. At low heat fluxes, hydrophobic surfaces can provide an early ONB and large nucleation site density owing to the lower energy barrier [9, 10]. At high heat fluxes, the formation and expansion of a vapor blanket resulting from the merge of the dense bubbles prevents further enhancing the CHF. However, hydrophilic surfaces can drive a small bubble diameter and a rapid bubble departure frequency, as well as an effective liquid rewetting, resulting in a high CHF value. Additionally, hydrophilicity is generally linked to surface morphology, which can offer a large surface area and a large number of nucleation sites. The surrounding liquid is effectively forced driven into the bottom of the bubbles due to the strengthened capillary force on the hydrophilic surfaces, causing bubbles to quickly release before merging into vapor films and increasing the effectiveness of heat removal. Nanoscale structures such as nanopores [11-15], nanowires [4, 16, 17], and nanotubes [18-20] can increase the capillary pressure for liquid rewetting. However, using the nanoscale structures with too small pores may obstruct flow paths and decrease liquid permeability, leading to the vapor bubbles coalescence. On the contrary, microscale structures involving microchannels [21-23], micro-fins [24-26], micro pillars [27-30], and micro porous [31-35] can facilitate liquid permeability, but reduce the capillary

pressure in the meantime. Thus, the combination of nano- and microscale structure would be ideal to optimize the pool boiling heat transfer performance [36-40]. When building a micro-/nanoscale structure, the best approach should be required to improve the capillary-assisted transport of liquid and to simultaneously increase the flow paths. Using this novel approach to enhance pool boiling heat transfer, the micro-/nanoscale structures involving microchannel with nanowires [41-43], microchannel with porous [40, 44, 45], and micro-/nanoscale porous [46, 47] have been widely investigated due to their superior liquid permeability and capillary pumping capability. For example, Lee et. al [42] designed a micro-nano hybrid structures that microcavities could serve as the bubble nucleation sites and nanowires provided the capillary pressure for liquid replenishment. This combined effects of the microcavities and nanowires can enhance the CHF by delaying bubble mergence and maximizing the bubble nucleation site density. Patil et. al [44] also proposed a fin-tops electrodeposited porous microchannel to enhance pool boiling heat transfer through altering the bubble growth and departure process. It was possible to create a micro convection so that bubbles rising from the fin tops caused vigorous liquid circulation in the microchannel. Due to the controlled bubble generation and departure, as well as the strengthened liquid replenishment for rewetting active nucleation sites, pool boiling heat transfer process was further improved. Moreover, hierarchical structures that have the artificial microcavities and micro-/nano pores can significantly optimize the boiling heat transfer performance because of the improved bubble nucleation, strengthened capillary pressure as well as increasing flow paths on the nanoengineered surfaces. Li et. al [48] proposed an ultra-scalable three-tire hierarchical Cu nano engineered surfaces by using electrochemical deposition for optimizing the boiling heat transfer. Through multiple-pronged strategy, including raising the nucleation site density, regulating bubble behavior and expanding liquid-vapor separation pathways, the structure length scale can be adjusted to enhance pool boiling heat transfer. For improving boiling heat transfer, Wen et. al [49] also created a two-level hierarchical Cu nanowires framework with patterned nanowire arrays. Long nanowire arrays' capillary pumping can act as continuous feeder channels to rewet active nucleation sites, increasing the CHF, while microcavities between short nanowires can provide high-density nucleation sites for increasing the HTC and decreasing the ONB.

However, most fabrication methods such as electrochemical deposition, chemical vapor deposition, chemical etching and sintering of the above-mentioned micro/nano structures are complex, which restrain their effective applications in different conditions. Due to its ease of use, low cost, and environmental friendliness, the solution immersion technique has recently been regarded as a viable method for producing nanostructures on metal surfaces. These surfaces also have potential in applications for pool boiling because of chemical stability and endurance under diverse serve circumstances. For instance, Kim et. al [50] fabricated super-hydrophilic aluminum surfaces through the solution immersion method, and explored the effects of surface roughness on the pool boiling heat transfer performance. As reported, the CHF was positively connected with the roughness within a particular range, but when the

roughness beyond that range, the hydrodynamic limit took effect. Boehmite nanostructures were discovered to have considerable advantages in improving the CHF and surface wettability [51]. It was found that, the aluminum surface induced an enhanced CHF ascribed to the highly stable super-hydrophilic properties. Moreover, CuO nanostructures using solution immersion method also has been tried to enhance pool boiling heat transfer. For example, Im et. al [52] presented low-profile, flower-like CuO nanostructures on a smooth surface and a microgroove surface, respectively. The results showed that the CHF was improved by at least 58% in different scenarios due to the increasing capillary wicking induced by their high surface area-to-volume ratio. Xie et. al [53] investigated the effect of the surface wettability on the boiling enhancement. The maximum CHF was increased by 68% by fabricating a dual-layer structure using nanograss as the substrate and micro flowers with varying covering densities as the superstructures. In addition, they have also looked into the combined effects of surface wettability and patterned nanostructures on boiling heaty transfer [54]. The results showed that the boiling curves are shifted to the left by patterned nanostructured surfaces, and the CHF rises as the density of the nanograss cover increases. Li et. al [55] investigated the wicking degeneration on nanoengineered surfaces and clarified the significance of absorbing ambient volatile organic compounds from air. The hierarchical micro/nanostructures that were highly scalable, conformal, cost-effective and with exceptional wicking abilities displayed great pool boiling heat transfer. Although previous studies have contributed to a basic understanding of the mechanism for improving boiling heat transfer based on micro- and nanocrystal structures, more analysis of the impact of crucial factors like the immersion time on surface modification and thermal promotion of nanoengineered surfaces is worthy to be investigated.

In this work, Cu surfaces were treated with solution immersion, a process that is both economic and environmentally benign, to produce nanocrystals. The formation process of in-situ growth of micro/nanocrystals on Cu surfaces is investigated. The morphological and chemical characteristics were characterized, and the impact of immersion time on surface wettability and morphology were investigated. Based on these, boiling heat transfer experiments has been done on nanoengineered surfaces with the in-situ hierarchical Cu micro/nanocrystals, by which significant thermal improvement has been achieved in wide-range experimental conditions.

2. Experimental sections

2.1 Sample fabrication and characterization methods

The manufacturing of boiling surfaces in this work involves three basic steps: washing, chemical alteration of surfaces, and vacuum drying. The whole copper surfaces of $20mm \times 20mm \times 3mm$ were polished with 2000 grid SiC sandpaper for removing the impurities on the surfaces. The polished copper surfaces were then scrubbed with an ultrasonic acetone solution for 15 minutes to get rid of the residue. Then, the polished surfaces were rinsed with the ultrasonic ethanol and DI water for 10

min, respectively. Finally, these copper surfaces were placed in an oven and heated at 65 ℃ for 10 min.

The experiment materials, sodium hydroxide (NaOH, AR, ≥ 96.0%) and ammonium persulfate ($(NH_4)_2S_2O_8$, AR, 98.0%) were purchased from the Sinopharm Chemical Reagent Co., Ltd. A 250 ml glass beaker holding the 100 ml aqueous solution of 2.5 M NaOH and 0.1 M $(NH_4)_2S_2O_8$ was used to prepare the 100 mL aqueous solution. The dried and polished copper surfaces were placed into the above solution at the room temperature for 3 min, 10 min, 60 min and 120 min, respectively. The reaction conditions are summarized in **Table 1**. The initial colorless solution in the glass beaker became increasingly blue. The manufactured copper surfaces were rinsed with DI water after the chemical alteration in the beaker and put into the vacuum oven to be heated at 60 ℃ to remove the leftover solution. After the chemical modification and vacuum drying, blue or dark blue colour appeared on the copper surfaces.

Table 1. Reaction conditions for the nanocrystals on the Cu substrate.

Sample	Concentration of $(NH_4)_2S_2O_8$ (M)	Concentration of NaOH (M)	Reaction time (min)
1	2.5	0.1	3
2			10
3			60
4			120

Scanning electron microscopy (SEM, Gemini 300, ZEISS, Germany) and atomic force microscopy (AFM, Dimension Edge, Bruker) techniques were applied to clearly identify the surface morphology properties of the Cu micro/nanocrystals and to investigate the growing thickness of the reaction products. Meanwhile, the energy-dispersive X-ray spectroscopy (EDS, INCA X-Act, Oxford) was used to get a quantitative analysis (Cu, O, C) of the reaction products on the Cu substrate. An X-ray photoelectron spectrometer (XPS, ESCALAB 250xi, America) was used to examine the sample's XPS spectra.

2.2 Wicking capability test system

Figure 1a shows the wicking capability test system including a micro-syringe pump, a lifting platform, a high-speed camera connecting with the computer and a light source. In this experiment, 1 μL DI-water droplet obtained from the micro syringe pump were released on the surfaces of samples. To observe the wicking phenomenon, a high-speed camera (Phantom, VEO 410) was set to record 1 s at 1000 fps for capturing the droplet spreading process. The micro-syringe was positioned 3 mm away from the boiling surfaces in order to minimize mistakes when the droplets drop onto the boiling surfaces. **Figure 1b** shows the captured image of droplet spreading and wicking. $\boldsymbol{R_f}$ represents the capillary wicking radius (from center to dynamic wicking liquid front) and $\boldsymbol{R_c}$ represents the droplet spreading radius (from center to contact line). The wicking distance l is the distance between $\boldsymbol{R_f}$ and $\boldsymbol{R_c}$. The wicking distance can be defined as

follows [56]:

$$l = \sqrt{\frac{2P_{cap}}{K}t} = W\sqrt{t} \quad (1)$$

where P_{cap} is the capillary pressure, K is the permeability and W is the wicking coefficient. Through analyzing the high-speed images, the wicking distance can be measured and wicking coefficient can be calculated according to equation (1).

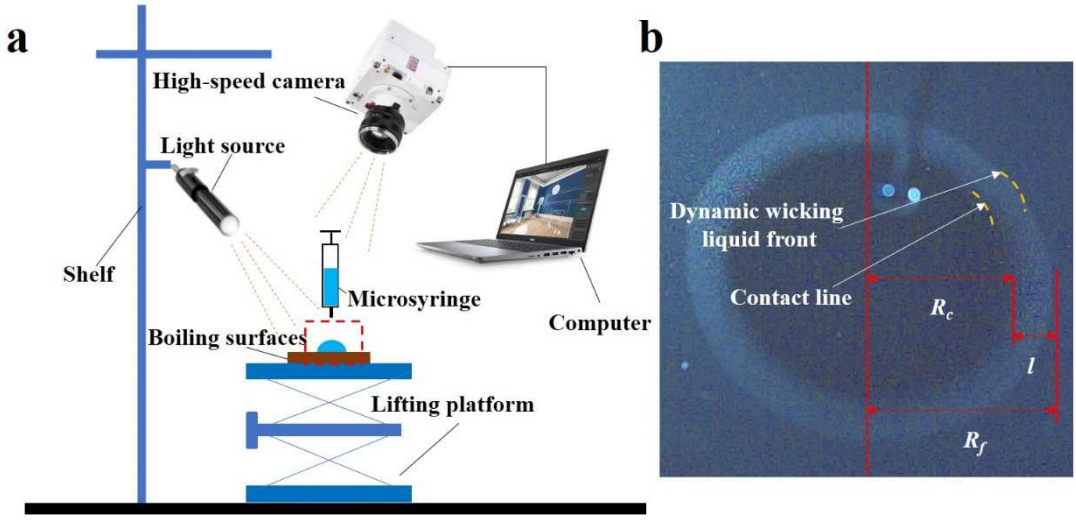

Figure 1. (a) Schematic of wicking capability experiment, (b) Captured high-speed camera images

2.3 Pool boiling experimental setup

Figure 2a shows the schematic diagram of pool boiling experimental setup. It consists of a boiling chamber, a heating system, an auxiliary heating system, a condensing system, a viewing system, a data gathering system. The working fluid was DI water, and the boiling chamber was constructed of quartz glass with a thickness of 5 mm. To keep the saturation of the DI water under 1 atm, an auxiliary heater that is submerged in the DI water was attached around the PTFE block. A spiral tube was added on the boiling chamber for condensing the water vapor in order to maintain the liquid level of the DI water. The main body of the heating system was a copper block with three cartridge heaters embedded in the cylindrical bottom. And the copper block was integrated into the PTFE to maintain one-dimensional heat transfer. The cartridge heaters were connected to the DC power supply, and the DC power supply controlled by the AC autotransformer was responsible for the heating power of cartridge heaters.

As shown in **Figure 2a** and **b**, the copper block had a height of 183 mm height and the upper of copper block is a square column with a width of 20 mm. To measure the heat flux and temperature gradients in the vertical direction, nine holes with a diameter of 1 mm were drilled along the copper column at 7 mm intervals for placing the T-type thermocouples. These nine thermocouples were distributed on three planes of the

copper block, with three thermocouples on each plane. As shown in **Figure 2b** and **d**, the thermocouples (T_{21}, T_{22} and T_{22}) were placed in the holes with a depth of 10 mm along the center line of the copper block, which can be used to calculate the temperature gradient of the copper block. Also, the thermocouples (T_{11}, T_{12}, T_{13}, T_{31}, T_{32} and T_{33}) were placed in the holes with a depth of 7 mm, which can be used to calculate the surface temperature. **Figure 2b** shows the thermocouples' distribution. Another three thermocouples (T_{01}, T_{02} and T_{03}) were embedded on the top of the copper column (**Figure 2d**). The average temperature of each plane was represented by T_0, T_1, T_2 and T_3 from top to the bottom, respectively. Meanwhile, the temperature of DI water was measured by the thermocouple T_m. The data acquisition system (Keysight, DAQ 970A) recorded all the T-type thermocouples' temperature readings. Moreover, the high-speed camera also recorded bubble dynamics including nucleation, growth and departure.

As shown in **Figure 2e**, the sample was welded on the copper block using lead-free solder. First, the solder was melted by the soldering iron and cooled down to form a solder layer on the copper substrate. Second, controlling the power of DC power supply to heat the copper block until the surface temperature T_0 reaches the solder layer melting point of 227 °C. Third, the sample was pressed on the solder layer (0.1 mm thick) and a heavy object was placed on the sample until the surface temperature returns to the room temperature. The contact thermal resistance of solder layer can be neglected because it only accounts for less than 1% of the total resistance [57], which also has been proved in the existing research [35, 58]. In addition, to prevent the heat losses from the gap between the PTFE and sample, a silicon sealant was used to fill this gap on the surface border (**Figure 2f**).

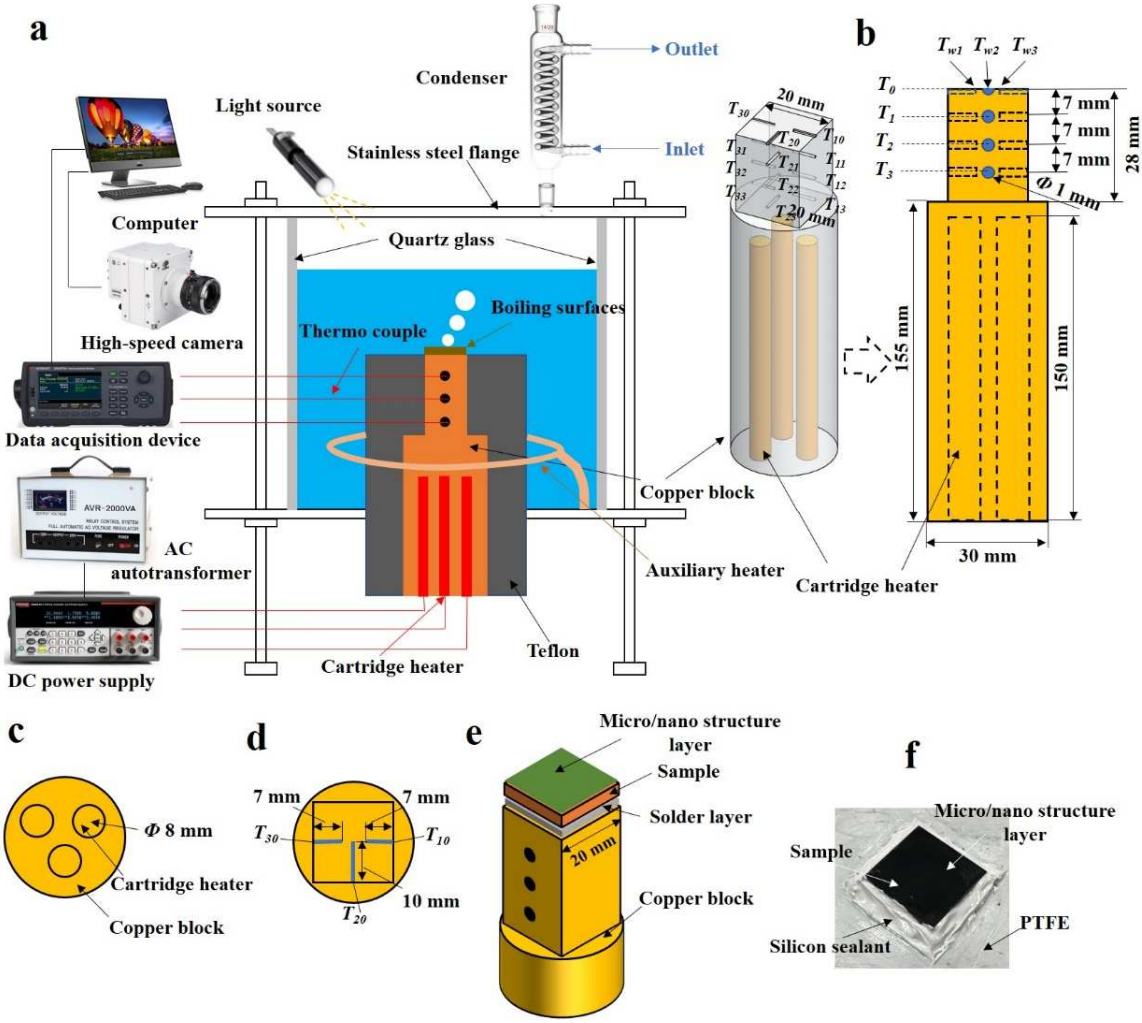

Figure 2. (a) Schematic diagram of pool boiling experimental setup (b) Front view of copper block (c) Distributions of the cartridge heater inside copper block (d) Top view of copper block (e) Sample installation (f) Sample with silicon sealant

2.4 Test procedures and data reduction

Prior to the pool boiling tests, DI water was heated by the auxiliary heater to the saturation temperature (T_{sat} = 100 °C) for roughly 60 min to release extra gas. The voltage was then gradually increased to the cartridge heaters in order to improve the heat flux of the boiling surfaces. The temperature reached a stable level following each incremental voltage increase after around 15 min. Every 1 minute, the temperature was measured, and each thermocouple's temperature variation was less than ± 0.2 °C. When the surface temperature exhibited the significant rise at one point, the CHF phenomenon could occur. W In order to protect the PTFE block, the experimental devices were turned off after the CHF reached.

Before calculating the heat flux, one-dimensional heat transfer along the copper block should be verified. **Figure 3a** shows the temperature distribution (T_1, T_2 and T_3)

along the copper block measured by the thermocouples at different heat fluxes. As shown in **Figure 3a**, the R-square values obtained from the linear curves fitting are all higher than 0.99. Thus, the radial heat loss from the copper block can be neglected and the heat flux calculated from the T_1, T_2 and T_3 is effective. Otherwise, the linear curve cannot fit the experimental data. **Figure 3b** show the comparison between the imposed heat flux based on the corresponding heating power of cartridge heaters and the heat flux estimated from the linear curve according to the experimental data from 4 tests of smooth surface, indicating that the heat losses are less than 10%.

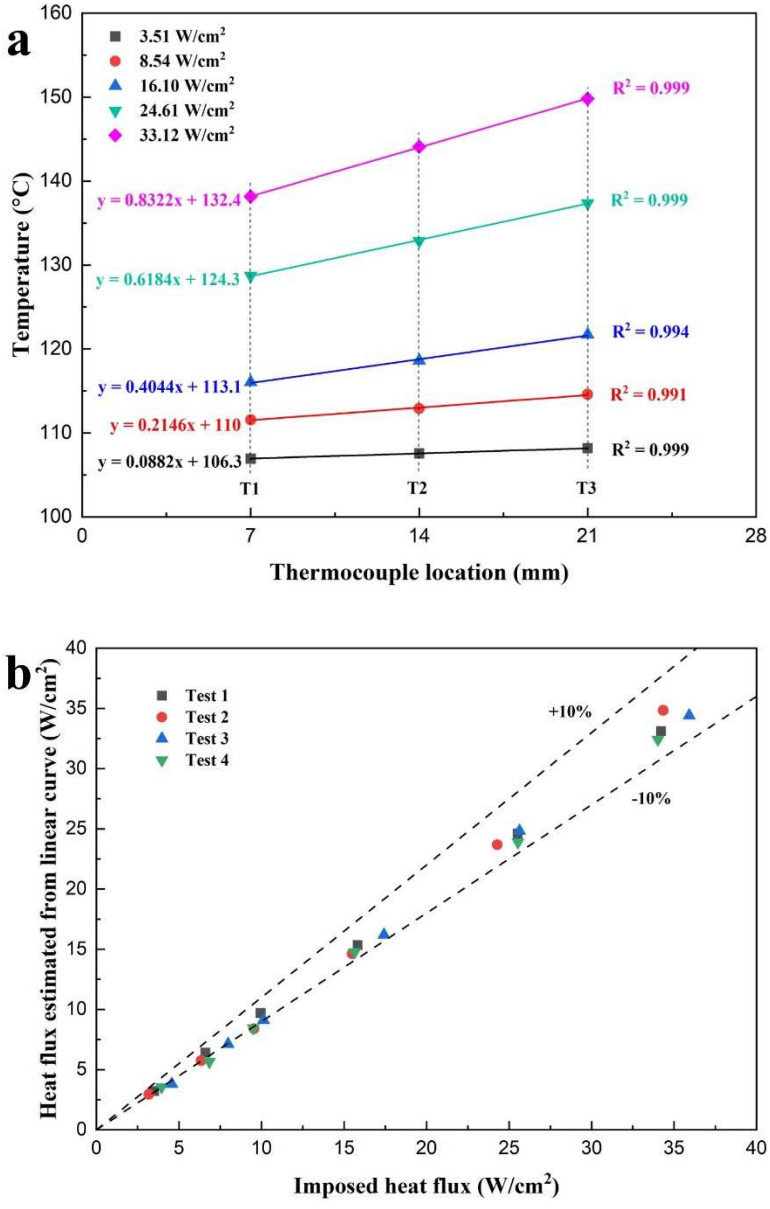

Figure 3. (a) Temperature distribution at different heat fluxes (b) Comparison between the imposed heat flux corresponding to heating power of cartridge heaters and heat flux estimated from linear curve

By one-dimensional Fourier's law, the input heat flux q can be calculated as follows:

$$q = -\lambda_{Cu}\frac{dT}{dz} \tag{2}$$

where λ_{Cu} is the thermal conductivity of the pure Cu, dT/dz is the axial temperature gradient of the Cu block determined by the three thermocouple readings, Δz is the distance between two thermocouple locations.

Utilizing the three points backward Taylor's series approximation, the temperature gradient in the copper block was determined.

$$\frac{dT}{dx} = \frac{3T_{21} - 4T_{22} + T_{23}}{2\Delta x} \tag{3}$$

where T_{21}, T_{22} and T_{23} are the temperatures along the center line of the copper block.

The local surface temperatures can be calculated based on the Fourier's theory and uniform intervals as follows:

$$T_{w1} = T_{11} - \frac{T_{13} - T_{11}}{2} \tag{4}$$

$$T_{w3} = T_{31} - \frac{T_{33} - T_{31}}{2} \tag{5}$$

Also, T_{w2} can be calculated based on the temperature gradient through T_{21}, T_{22} and T_{23}. Therefore, the surface temperature T_w can be calculated by average value (T_{w1} + T_{w2} + T_{w3})/3.

Herein, the HTC (h) can be determined as follows:

$$h = \frac{q}{T_w - T_{sat}} \tag{6}$$

where Δz_0 is the distance between the top surface, T_w is the boiling surface bottom temperature; T_{sat} is the saturated temperature of the working fluid.

2.5 Uncertainty analysis

The absolute errors for the calibrated T-type thermocouples were 0.2 °C. Copper's thermal conductivity was calculated to be 398 W/m·K, and the thermocouple location errors were determined to be 0.2 mm. The uncertainties of heat flux, heat transfer coefficient, and superheat were calculated using conventional method as follows in accordance with the error-propagation law:

$$\frac{U_q}{q} = \sqrt{\left(\frac{U_{\lambda_{Cu}}}{\lambda_{Cu}}\right)^2 + \left(\frac{3U_{T_1}\cdot\lambda_{Cu}}{\Delta z\cdot q}\right)^2 + \left(\frac{4U_{T_2}\cdot\lambda_{Cu}}{\Delta z\cdot q}\right)^2 + \left(\frac{U_{T_3}\cdot\lambda_{Cu}}{\Delta z\cdot q}\right)^2 + \left(\frac{U_{\Delta z}}{\Delta z}\right)^2} \tag{7}$$

$$\frac{U_{\Delta T}}{\Delta T}=\sqrt{\left(\frac{U_{T_1}}{T_1}\right)^2+\left(\frac{U_q}{q}\right)^2+\left(\frac{U_{\lambda_{Cu}}}{\lambda_{Cu}}\right)^2+\left(\frac{U_{\Delta z}}{\Delta z}\right)^2+\left(\frac{U_{T_{sat}}}{T_{sat}}\right)^2} \quad (8)$$

$$\frac{U_h}{h}=\sqrt{\left(\frac{U_q}{q}\right)^2+\left(\frac{U_{\Delta T}}{\Delta T}\right)^2} \quad (9)$$

The maximum uncertainties of the heat flux, heat transfer coefficient, and wall superheat for this pool boiling experimental system were ± 48 kW/m^2 (8 %), ± 15 kW/m^2·K (12 %) and ± 0.6 K (9 %), respectively.

In addition to the above-mentioned uncertainty analysis, the uncertainty in measuring the bubble size is also required to be considered. In general, the uncertainty in measuring the bubble size generates from two factors: dimension conversion when converting the pixel size into actual size, and measurement error when measuring the bubble size in the bubble visualization image manually. Due to these two factors, the total uncertainty in measuring the bubble size is about 10% [59].

3. Results and discussions

3.1 Surface morphology characterization

Figure 4 illustrates the top view micro/nanostructures of the different samples. The immersion time has a clear effect on the growth of the different micro/nanostructures on the Cu substrate. As shown in **Figure 4a**, when the immersion time was short (3 min), the Cu substrate was mainly covered by uniform and dense nanograss (NG). Increasing the immersion time to 10 min, nanograss tips can be inter-wined with each other, forming the micro-petals on the top of the nanograss (**Figure 4b**). This nanograss and micro-petals (NGMP) coexist almost half and half on the surface. When further increasing the immersion to 60 min, the micro-petals on the nanograss could be synthesized to the micro-flowers (NGMF), the Cu substrate was covered by one-layer nanograss and one-layer micro-flowers, as illustrated in **Figure 4c.** Compared with the micro-petals, more uniform micro-flowers with a diameter of around 4 μm could be formed on the top of nanograss. The nanograss under the micro flowers were sticked firmly on the Cu substrate, as seen in **Figure 3c.** As shown in **Figure 4d**, increasing the immersion time to 120 min, the micro-flowers maintained almost unchanged, and the Cu substrate was covered by one-layer nanosheets and one-layer micro-flowers (NSMF).

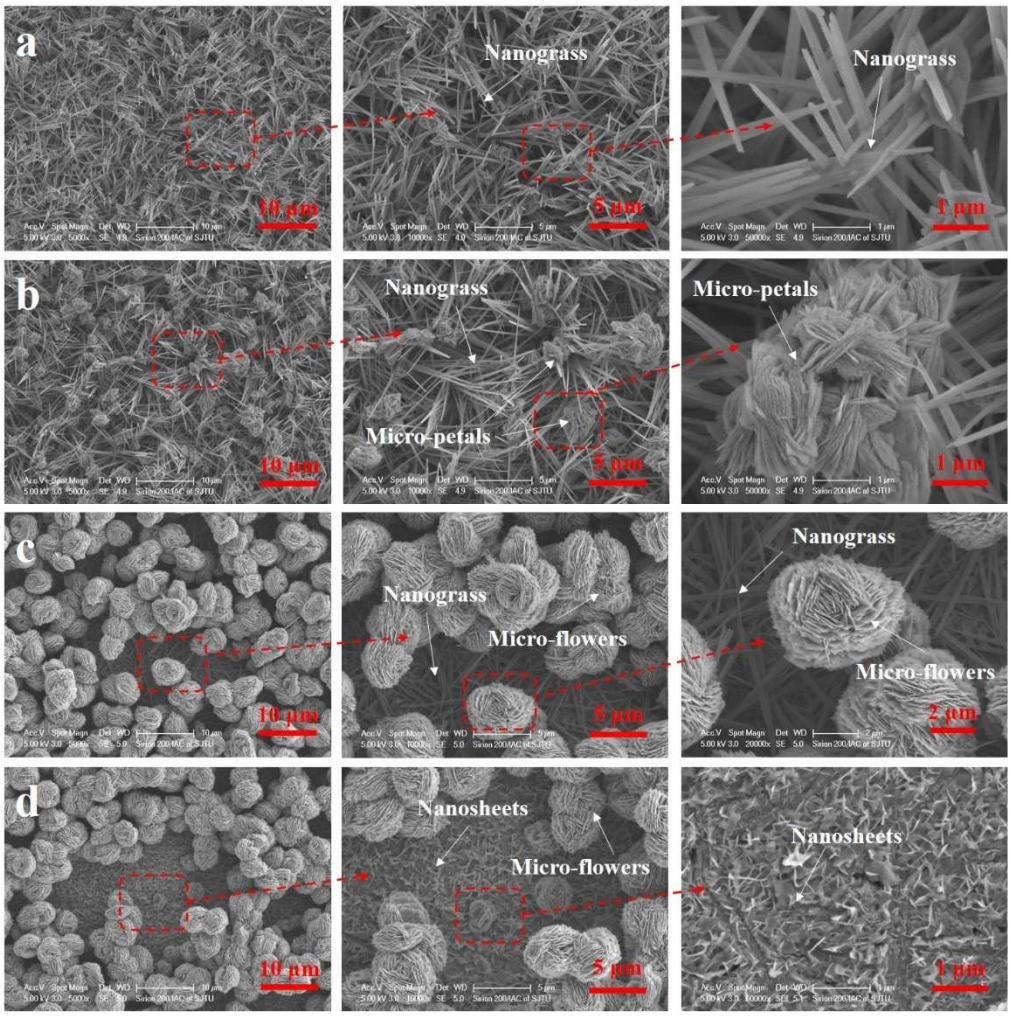

Figure 4. Top view SEM images of (a) NG, (b) NGMP, (c) NGMF, (d) NSMF.

Figure 5 shows the side cross-sectional view SEM images of the different samples. As shown in **Figure 5a**, the dense nanograss were found to have grown grass-like structure on the Cu substrate and the thickness of this nanograss is about 0.9 μm. As seen in **Figure 5b**, micro-petals were found to have grown on the nanograss tips due to the longer immersion time for synthesis and the thickness of this hierarchical structure was around 4.7 μm. In **Figure 5c**, the micro-petals synthesized to the larger micro-flowers and the nanograss seemed to disappear under the micro-flowers because of the firm stick on the Cu substrate. The thickness of this hierarchical structure was 4.9 μm. Similar micro-flowers were found in **Figure 5d** to have grown on the Cu substrate and a large amount of micro-flowers stacked on top of each other, resulting in the larger thickness of 5.0 μm. Surface roughness of untreated, NG, NGMP, NGMF and NSMF samples was measured by the AFM method (**Figure 6**). Due to the previous polishing, the untreated sample exhibited a flat surface (**Figure 6a**). It was clear that the immersion process caused surfaces to gradually generate and increase rough nanoscale features (**Figure 6b**, **c**, **d** and **e**).

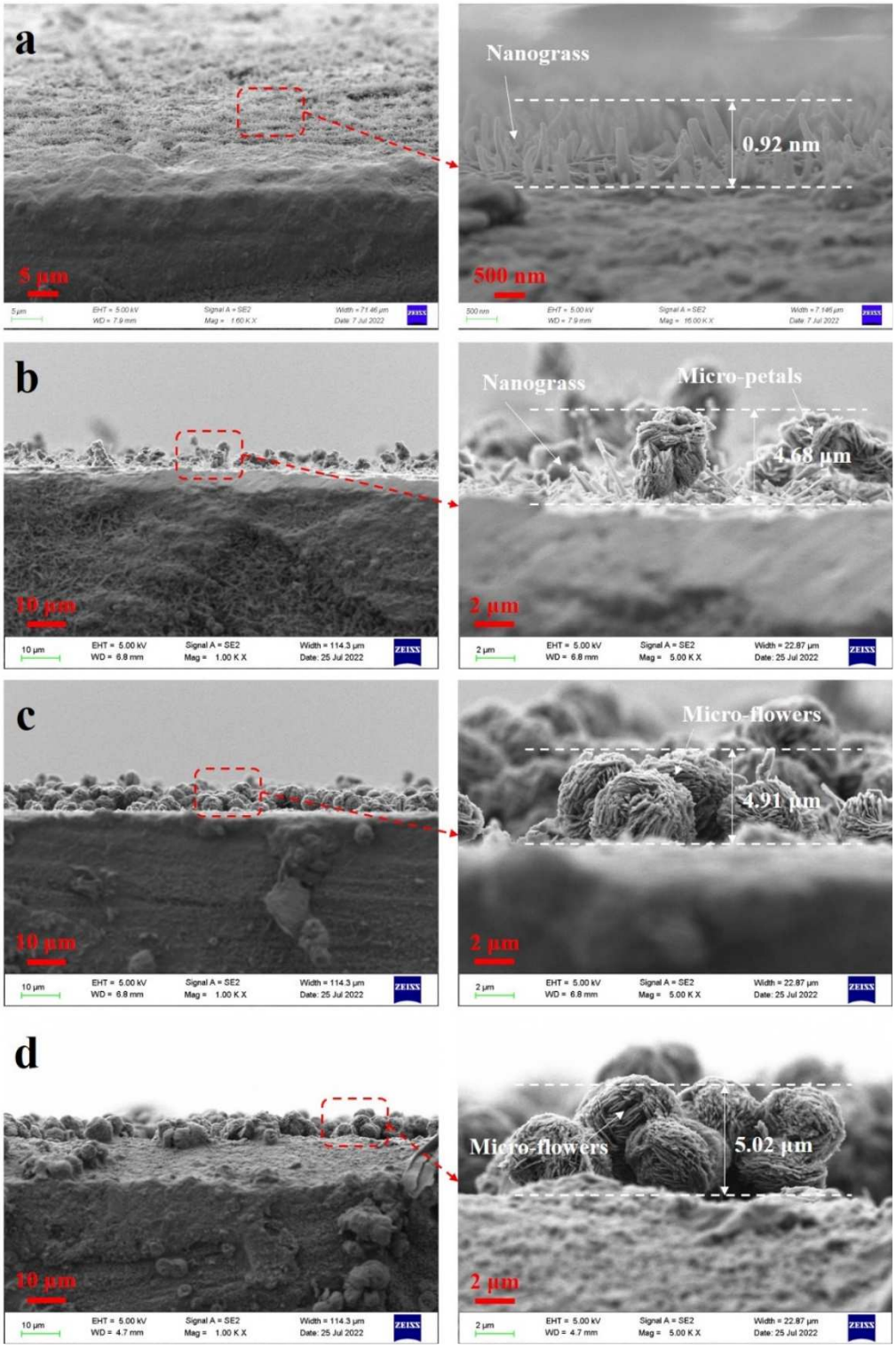

Figure 5. Side view SEM images of (a) NG, (b) NGMP, (c) NGMF, (d) NSMF.

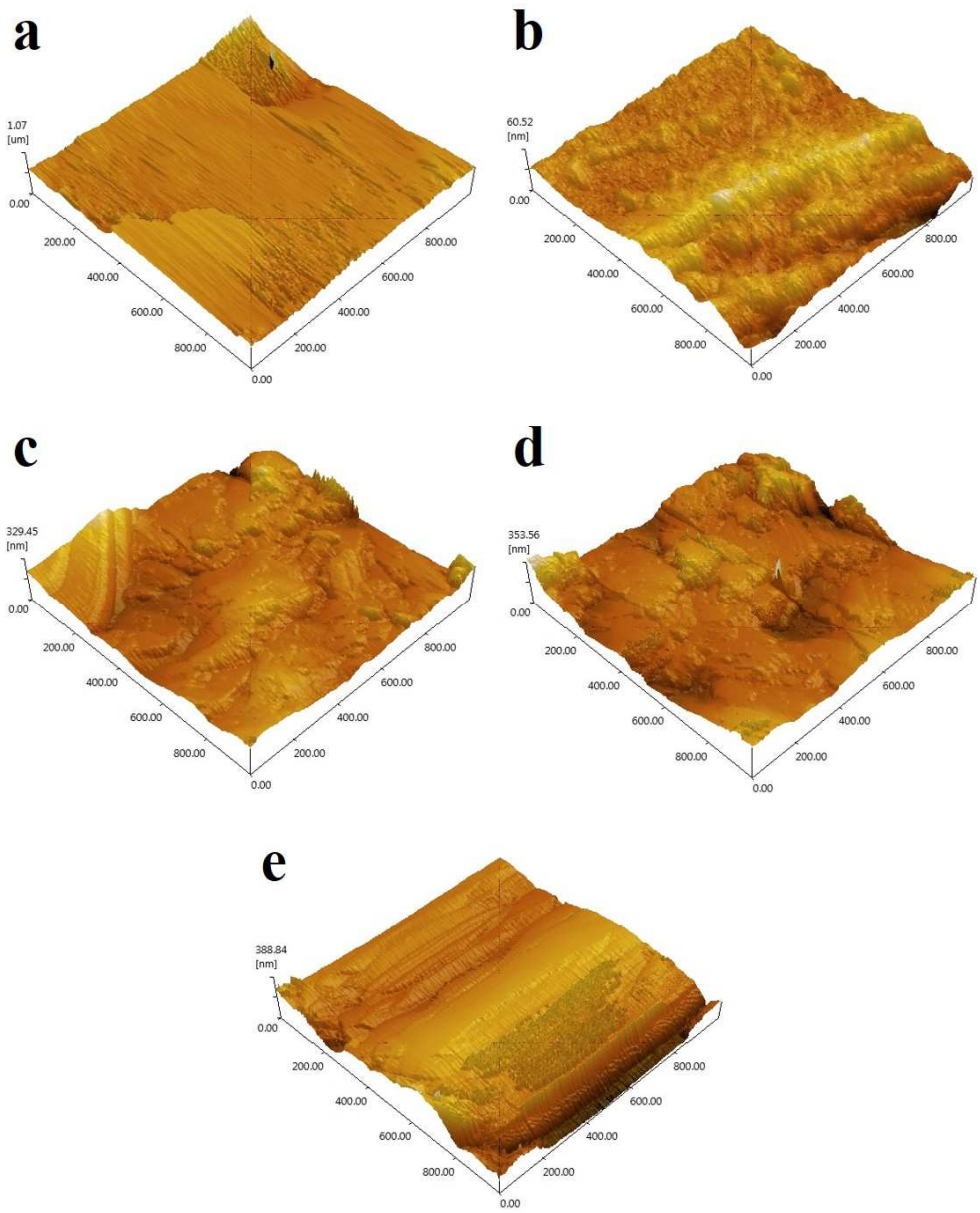

Figure 6. AFM images showing the topography of (a) Untreated, (b) NG, (c) NGMP, (d) NGMF, (e) NSMF.

3.2 Surface compositions

Figure 7a shows the XPS spectrum of the samples, which indicates that the presence of the Cu and O as well as the absence of any impurities at various surfaces. As shown in **Figure 7b**, the high-resolution XPS spectrum of Cu 2p, which includes Cu $2p_{1/2}$ and Cu $2p_{3/2}$ peaks, as well as the Cu^{2+} satellite features, indicating the presence of Cu^{2+} in the samples. Further analyzing the surface compositions using XRD, as shown in **Figure 7c**, the peaks shown by as asterisk can be referenced to the cubic phase of copper (JCPDS card 01-1242). The diffraction peaks for the NG structures were indexed to the phase of orthorhombic $Cu(OH)_2$ (JCPDS 14-0420). The XRD diffraction peaks were

for the NGMP, NGMF and NSMF hierarchical structures indexed to the monoclinic CuO (JCPDS card 5-0611).

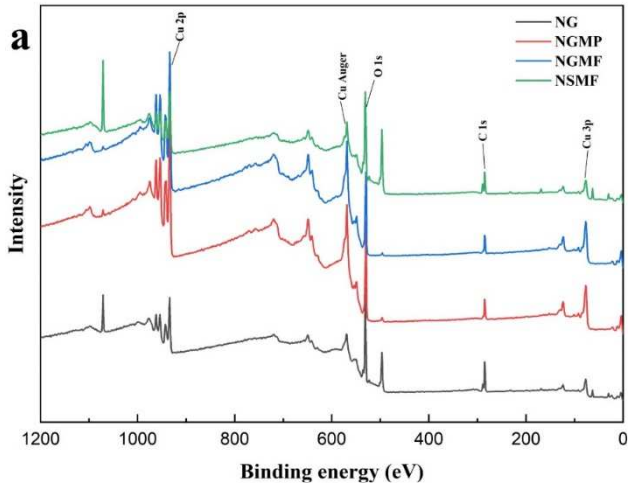

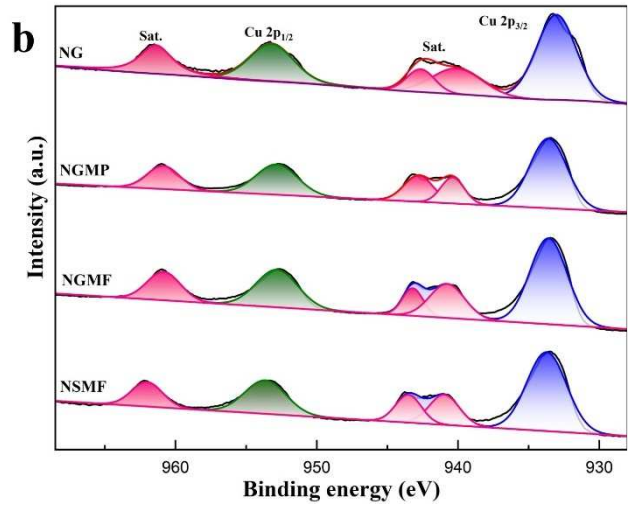

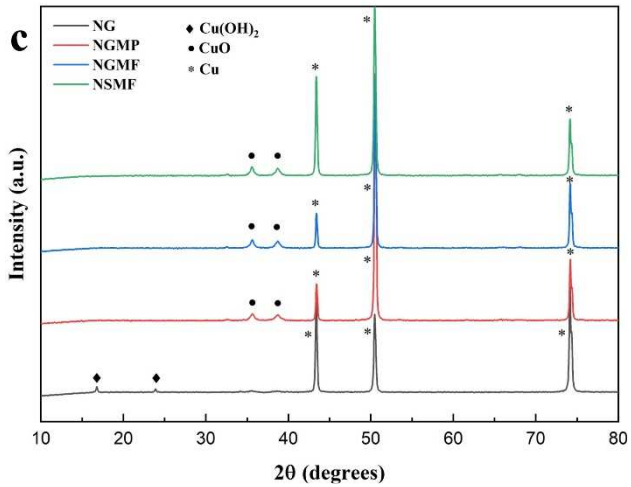

Figure 7. (a) Survey XPS spectrum, (b) High-resolution XPS spectrum of Cu, (c) XRD patterns of the samples.

3.3 Validity of experimental system

The boiling curve for a smooth surface is checked with correlations and experiments from the literature to ensure the validity of the experimental setup. For determining the dependability of the experimental system, three traditional correlations from the literature are used to estimate the pool boiling heat transfer on the smooth surface. The Rohsenow's correlation is expressed as below:

$$\frac{c_{p,f}\Delta T_{sat}}{h_{fg}} = C_{sf}\left[\frac{q''}{\mu_f h_{fg}}\sqrt{\frac{\sigma}{g\left(\rho_f-\rho_g\right)}}\right]^{0.33}\left(\frac{c_{p,f}\mu_f}{k_f}\right)^{n} \tag{10}$$

where $C_{s,f}$ = 0.0152 and n = 1, and Pioro's correlation can be expressed as,

$$\frac{q''}{\Delta T_{sat}k_f}\sqrt{\frac{\sigma}{g\left(\rho_f-\rho_g\right)}} = C_{sf+}\left\{\frac{q''}{h_{fg}\rho_g^{1/2}\left[\sigma g\left(\rho_f-\rho_g\right)\right]^{1/4}}\right\}^{2/3}\left(\frac{c_{p,f}\mu_f}{k_f}\right)^{m} \tag{11}$$

where C_{sf+} = 1228 and m = -1.1. And CHF value can be calculated by the Zuber's correlation, which can be expressed as follows,

$$q''_{CHF} = \frac{\pi}{24}\rho_g h_{fg}\left[\frac{\sigma g\left(\rho_f-\rho_g\right)}{\rho_g^2}\right]^{1/4} \tag{12}$$

In addition, Kandlikar proposed a theoretical approach for CHF estimation considering the surface wettability, which can be expressed as follows:

$$q''_{CHF} = h_{fg}\rho_g^{0.5}\left[\sigma g\left(\rho_l-\rho_g\right)\right]^{1/4}\frac{1+\cos\theta}{16}\left[\frac{2}{\pi}+\frac{\pi}{4\left(1+\cos\theta\right)}\right]^{0.5} \tag{13}$$

Figure 8 shows the boiling curve of this study has a closely agreement with the correlations at the low heat flux. Nevertheless, the CHF value of smooth surface in this study has the large variation compared with the correlations. In general, the mechanisms causing CHF can be broadly classified as far-field hydrodynamic theory and near-field surface property theory. Therefore, there are at least four different models of CHF: (1) Zuber column Helmholtz-Taylor instability model [60], (2) Lienhard and Dhir column Helmholtz-Taylor instability model [61], (3) Macrolayer dryout model [56, 62, 63], (4) Hot/Dry spot model [64]. The CHF of smooth surface obtained from the Zuber's correlation ($CHF_{Zuber's}$) is 100 W/cm^2. Here note that the Zuber's correlation is established on the condition of the infinite surface without considering the surface properties [65]. Considering the size effect on the CHF, Lienhard and Dhir proposed that the heater size can affect the CHF via reducing the number vapor columns present on the heater surface. The correlation can be expressed as follows:

$$q''_{CHF} = 1.14 \times q_{CHF,Zuber's} \times \left(\frac{N_j \times \lambda_D^2}{A_s} \right) \quad (14)$$

where $q_{CHF,\ Zuber's}$ can be obtained from the Zuber's correlation. N_j is the number of vapor columns on the surface, λ_D is the Taylor instability wavelength and A_s is the heater area. However, this correlation can only be applied when the heater size is much larger than the critical wavelength λ_D = 25 mm. As listed in Table 2, most actual experimental heater size is smaller than the wavelength λ_D, resulting in one vapor column presented on these surfaces. Therefore, the Zuber's and size effect correlation proposed by the Lienhard and Dhir cannot represent the CHF of the actual experimental surfaces. In addition, the CHF of the surface is affected by the surface wettability, surface roughness, surface morphology, thermal conductivity and et. al [66, 67]. As shown in **Figure 8**, the contact angle of Cu smooth surface in this study is about 109°, exhibiting the hydrophobicity and no liquid wicking and spreading effect on the surface.

Considering the effect surface wettability on the CHF, the CHF of Kandlikar's correlation is 47.7 W/cm^2 because the contact angle of smooth surface in this study is 109° (**Figure 8**). The CHF obtained from the Kandlikar's correction is slightly higher than 42.1 W/cm^2 that we measured. Comparing with the CHF of actual experiments listed in **Table 2**, the surface properties such as the surface wettability and surface roughness are the potential factors of these experimental errors [63]. As a result, the information collected by this experimental system can be trusted.

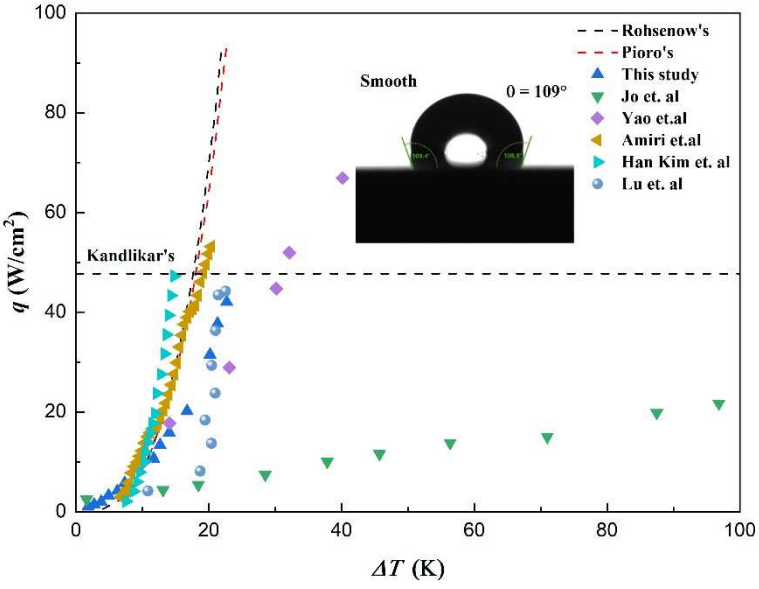

Figure 8. (a) Boiling curve comparisons of water on the smooth surface with Rohsenow's, Pioro's correlations, and literatures (b) CHF enhancement for surfaces with various sizes [17, 68-71]

Table 2. CHF values from the literature and present study

Ref	Material	Shape	*D* [mm]	CHF [W/cm^2]
[17]	Copper	Circle	30	20
[68]	Silicon	Square	10	65
[69]	Copper	Circle	15	53
[70]	Copper	Square	10	47
[71]	Silicon	Square	20	44.2
This study	Copper	Square	20	42.1

3.4 Pool boiling performance

Figure 9a depicts the saturated pool boiling curves on the smooth, NG, NGMP, NGMF and NSMF surfaces at 1 atm. Before the wall reaches a specific value of superheat, it is observed that the heat flux gradually increases, indicating the natural convection process. Beyond the critical point of the wall superheat, the heat flux increases significantly due to the occurrence of the nucleate boiling. The lower ONB, higher CHF, and higher HTC demonstrate that the structured surfaces exhibit significantly improved boiling heat transfer compared the smooth one in **Figure 9a**, **b** and **c**. The ONB among the entire structured surfaces appeared to be decreased from 9 K to less than 7 K, as indicated in **Figure 9a** (downward arrows). This is because that the micro-/nano-crystal surfaces can improve the nucleate site density, facilitating the bubble generation on the micro/nanostructures. All four structured surfaces exhibited higher CHF when compared with the untreated smooth surface, indicating that the presence of structures allows an improvement of the boiling heat transfer on surfaces. Even though the NG surface had the lowest CHF, it still had a greater CHF than a smooth surface had. Furthermore, the CHF on the smooth surface was lower than that on the hierarchical structures, which included NGMP, NGMF and NSMF, with the values of 55.4, 52.6 and 65.7 W/cm^2, respectively.

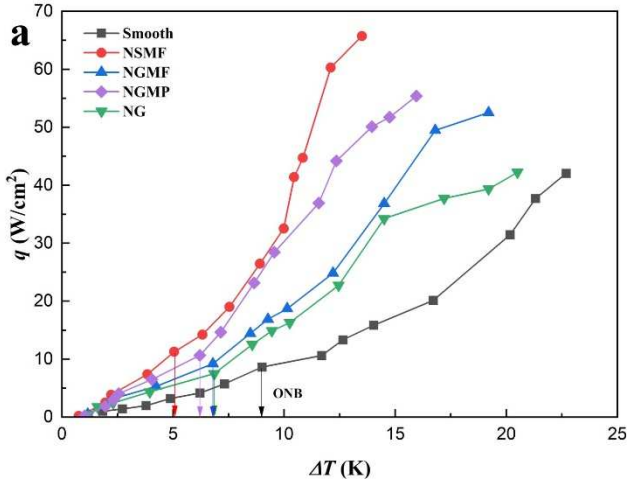

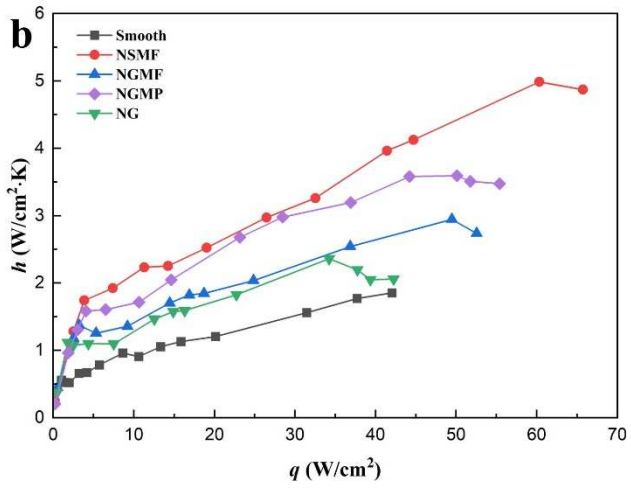

439

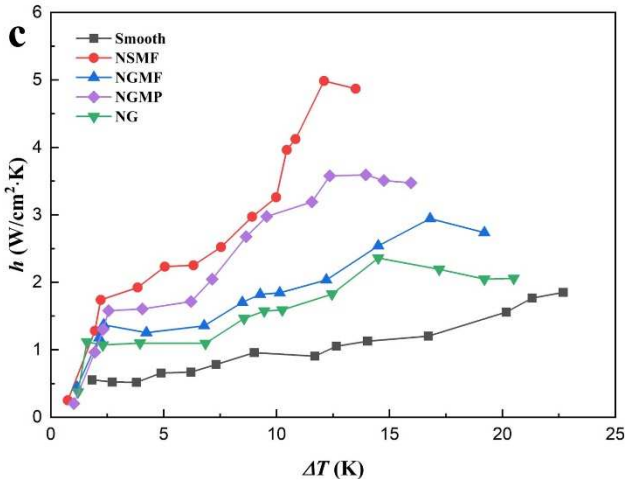

440

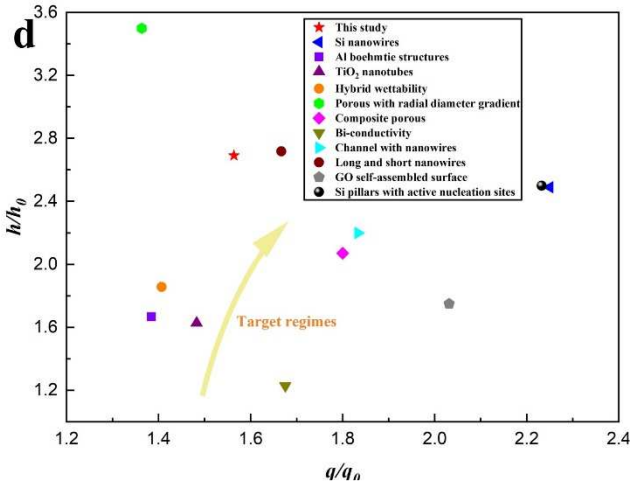

441

442 **Figure 9**. (a) Boiling curve of the samples; Heat transfer coefficient for samples as
443 functions of (b) wall heat flux and (c) wall superheat; Comparison of this study with
444 other studies of pool boiling on various surfaces.

445 According to **Figure 9b**, it was found that the HTC decreased gradually on NG,
446 NGMF or NGMP surfaces before the onset of the nucleate boiling when the heat flux
447 is low, in which scenarios the superheat was augmented rapidly. Moreover, the HTCs

of hierarchical structures involving NGMP, NGMF and NSMF were superior than that of the NG because of the multilevel morphology of the surfaces. Among the three hierarchical structures, the NSMF exhibited the highest HTC of 4.9 W/cm^{2}K compared to the NGMP and NGMF. As shown in **Figure 9c**, due to an early ONB with a much higher HTC and lower wall superheat, the hierarchical surfaces were attractive for thermal management of electronics, batteries and data center to diminish the safety issues raised due to the temperature rise in operational conditions.

Figure 9d compares the pool boiling performance of various enhancement surfaces investigated in previous literatures under 1 atm [10, 19, 45, 46, 49, 68, 72-76]. For better comparing the boiling performance on the various structured surfaces, we define two parameters h/h_0 and q/q_0 to evaluate the boiling heat transfer. Here h, h_0, q and q_0 represents the HTC of enhanced surfaces, HTC of smooth surface, CHF of enhanced surfaces and CHF of the smooth surface, respectively. As depicted, the most q/q_0 values reported in the literatures were in the range of 1.3 ~ 1.8, and the q/q_0 of the NSMF was comparable to 1.6. Nevertheless, the NSMF also had the higher HTC at CHF than the other experimental studies. Although few structures like porous with radial diameter gradient had the relatively high h/h_0, low q/q_0 also could be obtained compared with the data from this study. As comparisons, the hierarchical structures such as long and short nanowires, channel with nanowires, and Si pillars with active nucleation sites provide the similar parameters h/h_0 and q/q_0 compared with the NSMF, which has been proved to be the excellent structures for improving pool boiling heat transfer. As a result, the NSMF can concurrently improve the CHF and HTC, as well as reduce the ONB, which suggests that there is potentials for improving pool boiling heat transfer.

3.5 Bubble visualization and analysis

Figure 10 shows the bubble dynamics on the smooth, NG, NGMP, NGMF and NSMF surfaces. At a lower heat flux, smaller bubbles appeared on the NG, NGMP, NGMF and NSMF surfaces, and the bubble leaves the surface in nearly spherical shape. While isolated bubble may still be seen on the NGMP and NSMF surfaces, the bubbles above the smooth surface have merged into a single, huge bubble with a mushroom-like form as the heat flux increases. Nevertheless, the NG and NGMF surfaces also have began to bubble coalescence, but there is no mushroom bubble to be observed. It is possible to further activate the number of nucleation sites on the NG, NGMP, NGMF and NSMF surfaces. The bubble coalescence tendency becomes clear as heat flux increases. At the heat flux of about 36 W/cm^2, the bubbles above the smooth, NG, NGMP and NGMF surfaces have been merged into the large bubble in the mushroom shape, while the merged bubbles are still isolated from the NSMF surface. Therefore, the bubbles can grow and departure from the NSMF surface with faster speed, resulting in the more heat can be carried out from the surface.

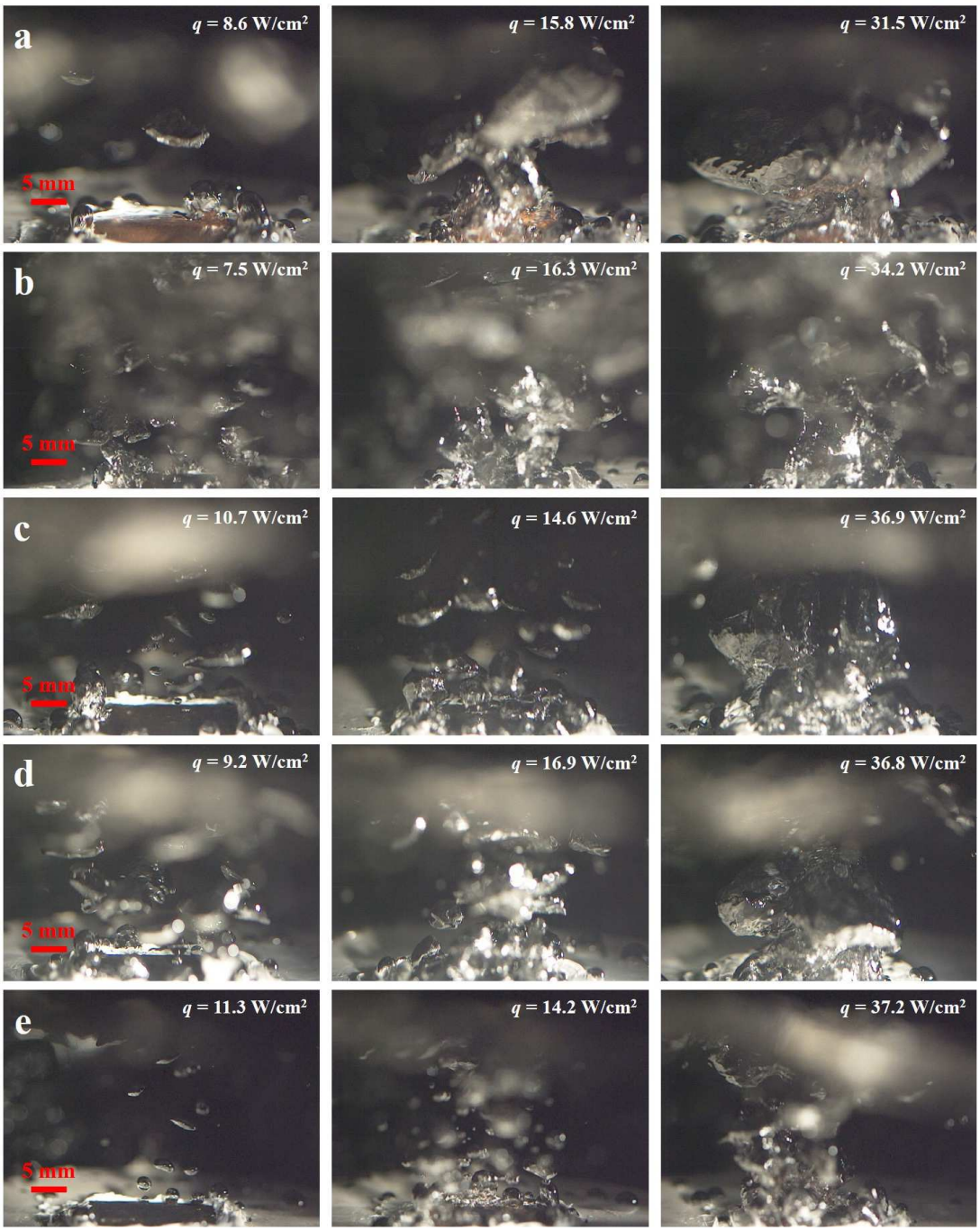

Figure 10. Bubble visualization images at $q \approx 10$, 15 and 35 W/cm^2 (a) smooth (b) NG (c) NGMP (d) NGMF and (e) NSMF

Figure 11 shows the bubble nucleation on the smooth, NG, NGMP, NGMF and NSMF surfaces at the ONB. As aforementioned, the wall superheat of smooth, NG, NGMP, NGMF and NSMG surfaces is 9, 6.9, 6.2, 6.8 and 5.1 K at the ONB, respectively. Comparing with the smooth surface, the structured surfaces including NG, NGMP, NGMF and NSMF have more bubble nucleation sites or small departure bubbles, indicating that the NG, NGMP, NGMF and NSMF surfaces can facilitate the bubble nucleation or bubble departure. Here note that the NSMF surface not only can

provide more bubble nucleation sites but also can facilitate bubble departure comparing with the other surfaces.

For further comparing the bubble nucleation on the NG, NGMP, NGMF and NSMF surfaces, we counted the bubble growth and departure periods using high-speed images at the ONB stage. The bubble diameter D_b is calculated by measuring the pixels of high-speed images. Following bubble nucleation, D_b grows significantly during the bubble growth process. Up until the bubbles have a diameter of D_d, the rate of rise in bubble diameter slows. At the same wall superheat, higher heat flux can be obtained on the NSMF surface, and the bubble growth period is shorter than it is on the other surfaces, as shown in **Figure 12a**, **b**, **c** and **d**. This is because that the rapid bubble nucleation and removal from the surface is advantageous for the support of liquid capillary wicking. Nevertheless, the NSMF surface has the smallest departure diameter D_d, while the NG surface has the largest D_d. The bubble departure frequency f increases because it is inversely related to the bubble departure diameter [77]. As a result, the NSMF surface can increase nucleation site density, decrease the bubble diameter and improve the bubble departure frequency, potentially leading to advances in the HTC and CHF.

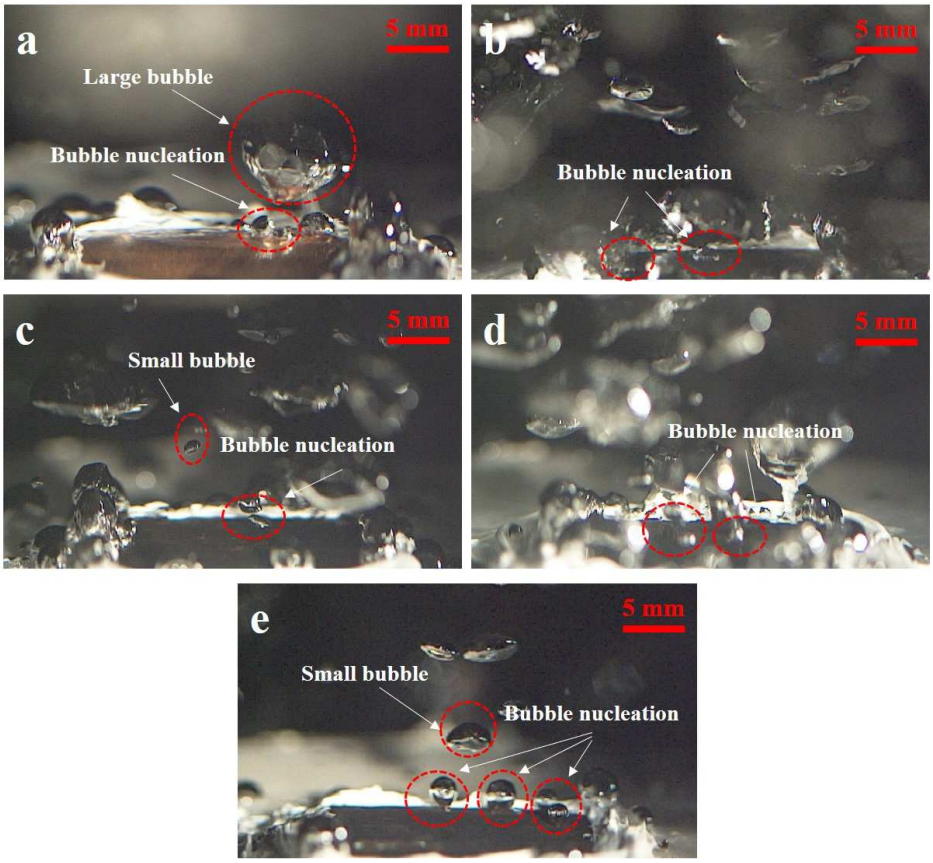

Figure 11. Bubble nucleation at the ONB for the (a) smooth, (b) NG, (c) NGMP, (d) NGMF, (e) NSMF

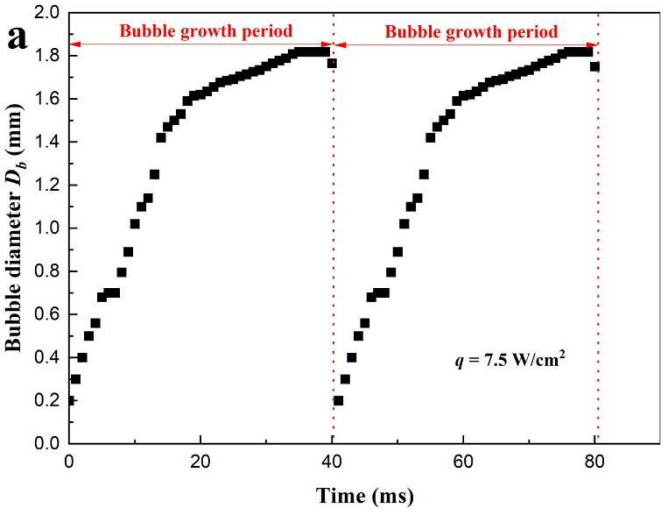
a
Bubble growth period
Bubble growth period
Bubble diameter D_b (mm)
Time (ms)
q = 7.5 W/cm^2

515

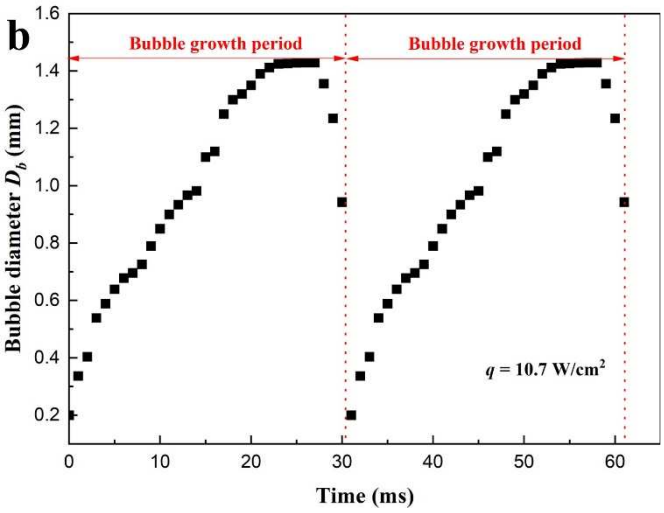
b
Bubble growth period
Bubble growth period
Bubble diameter D_b (mm)
Time (ms)
q = 10.7 W/cm^2

516

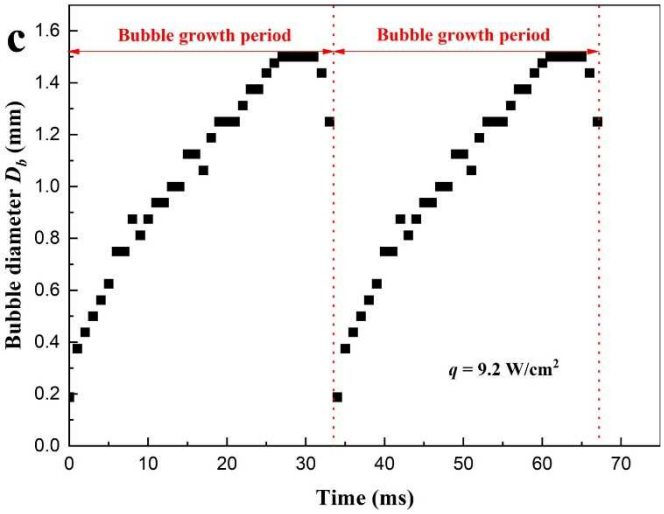
c
Bubble growth period
Bubble growth period
Bubble diameter D_b (mm)
Time (ms)
q = 9.2 W/cm^2

517

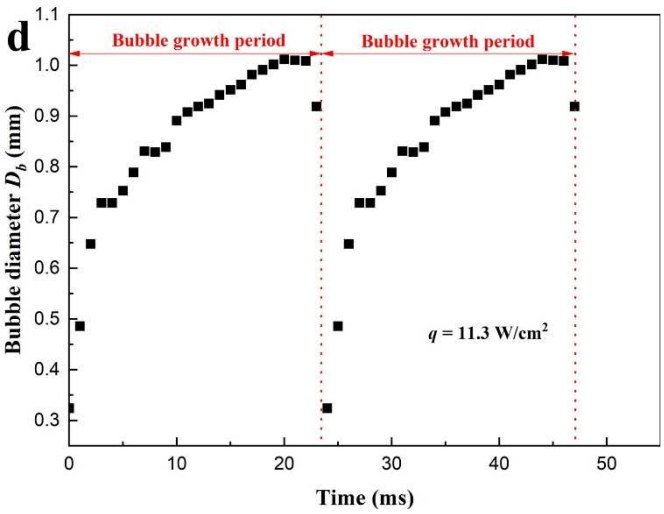

Figure 12. Bubble diameters during growth period on the (a) NG (b) NGMP (c) NGMF (d) NSMF.

As shown in **Figure 13**, the bubble nucleation sites can continue to be activated as the heat flux increases. We examined the isolated bubbles produced from the surfaces at low heat flux (q < 20 W/cm^2) to prevent fluctuation and evaporation of water during the observation. The bubble nucleation site density is observed to increase as the heat flux increases on the four different types of surfaces. However, the active nucleation sites of the NGMF and NGMP only minimally increase, indicating that the hierarchical structures NGMP and NGMF contribute less to the formation of the active nucleation sites. For the NSMF, it can be observed that the bubble nucleation site density increases significantly. As reported, for water at atmosphere, the essential bubble radius ranges from 0.8-16 μm at the wall superheat of 2 to 40 K [49]. As a result, the microcavities (5 ~ 15 μm) of the NSMF can be exploited as the effective nucleation sites. Because bubble nucleation is more likely to be activated and the nucleation site density is greatly increased at low superheat, the ONB can be reduced and the HTC can be enhanced. Small nucleated bubbles in the microcavities can absorb heat from the surrounding wall and expand more quickly due to the more activated nucleation sites resulting from the increased heat flux.

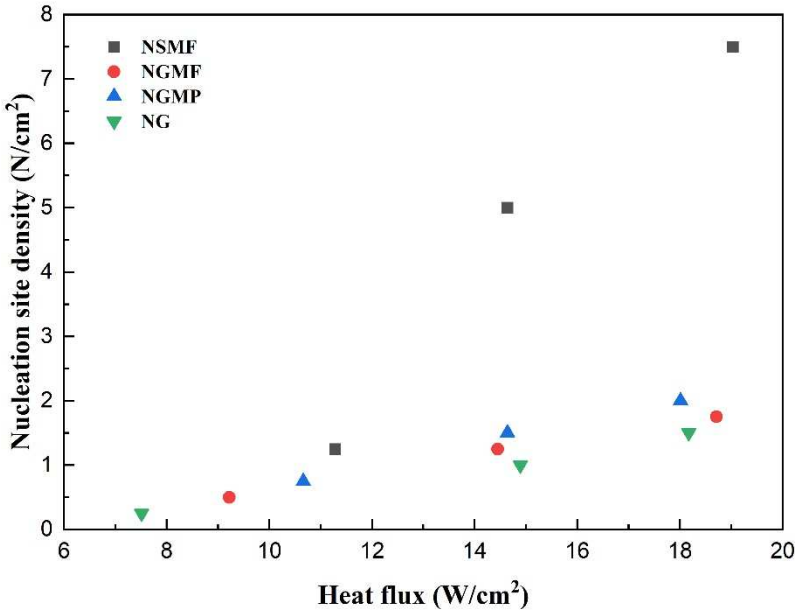

Figure 13. Nucleation site density of bubbles with the heat flux on the NG, NGMP, NGMF and NSMF

Figure 14 shows the average bubble departure diameter and frequency for the NG, NGMP, NGMF and NSMF surfaces at various low heat flux. As shown in **Figure 14a**, the bubble departure diameter increases with the increase of heat flux resulting from the enhanced evaporative rate in the superheated layer. The structure features of the NSMF result in a substantially smaller bubble departure diameter than those of the NG, NGMP and NGMF. As shown in **Figure 14b**, the bubble departure frequency on the NG, NGMP, NGMF and NSMF surfaces exhibits the upward trend with the increase of the heat flux. Meanwhile, the NSMF has the largest bubble departure frequency of all the surfaces. This may be because that the NSMF has the fastest liquid replenishing velocity for accelerating the bubble detachment and offering the liquid to generate the bubble continuously, thereby increasing the bubble departure frequency.

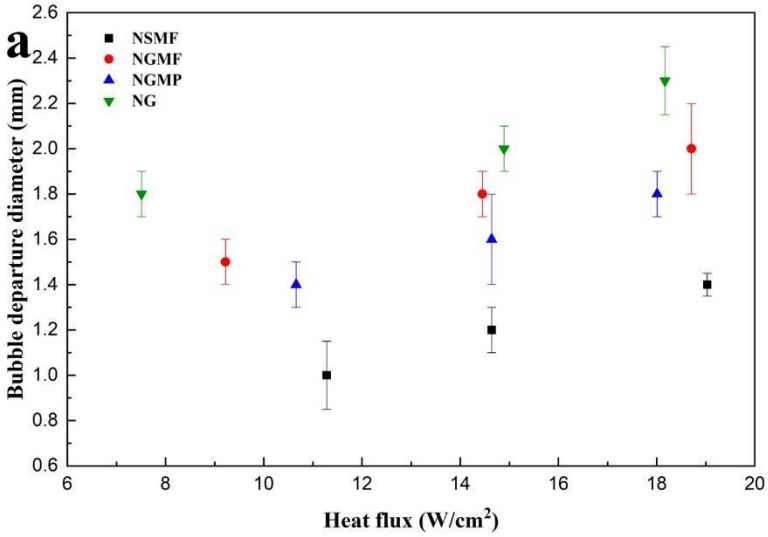

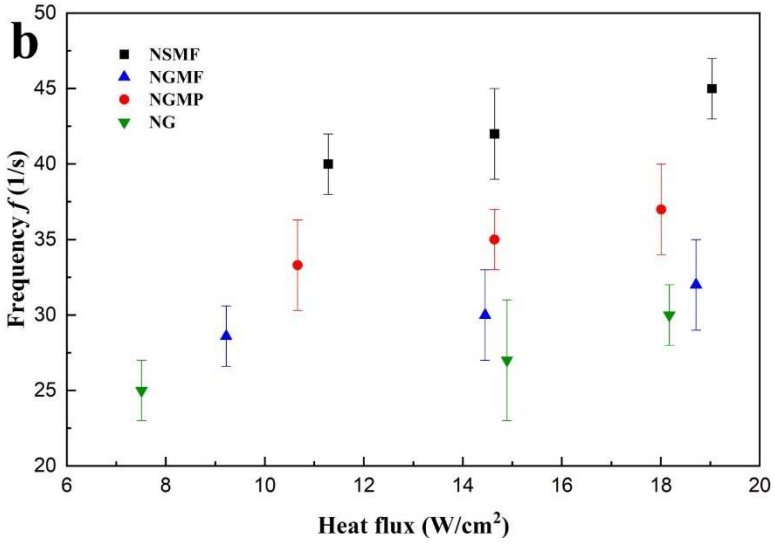

Figure 14. (a) Average bubble departure diameter (b) Average bubble departure frequency for the NG, NGMP, NGMF and NSMF

3.6 Effect of capillary wicking on boiling heat transfer

In order to evaluate the wetting properties of the samples, the droplet dynamic behavior on the sample surfaces was recorded. **Figure 15** shows the dynamic behavior of the droplet on the various surfaces. Before dropping the droplet, the initial height of the droplet was 4 mm, and the volume of the droplet was kept at 4 μL. As the droplet contacted the surface, the contact area between the droplet and the surface increased. As shown in **Figure 15a**, **b**, **c** and **d**, the droplet can entirely penetrate the NG, NGMP, NGMF and NSMF surfaces, indicating the super-hydrophilicity of these structured surfaces after the chemical modification. Moreover, after the same period time (4 s) of droplet spreading on the NG, NGMP, NGMF and NSMF surfaces, different wetted areas can be observed various surfaces, indicating different wetting properties of the NG, NGMP, NGMF and NSMF surfaces. As shown in **Figure 15d**, the NSMF surfaces exhibit the largest wetted area after the spreading time of 4 s, which illustrates the most excellent wetting properties among these structured surfaces. Therefore, the effect of the micro/nano structural characteristics on the surface wetting properties can be proved by the droplet dynamic behavior analysis.

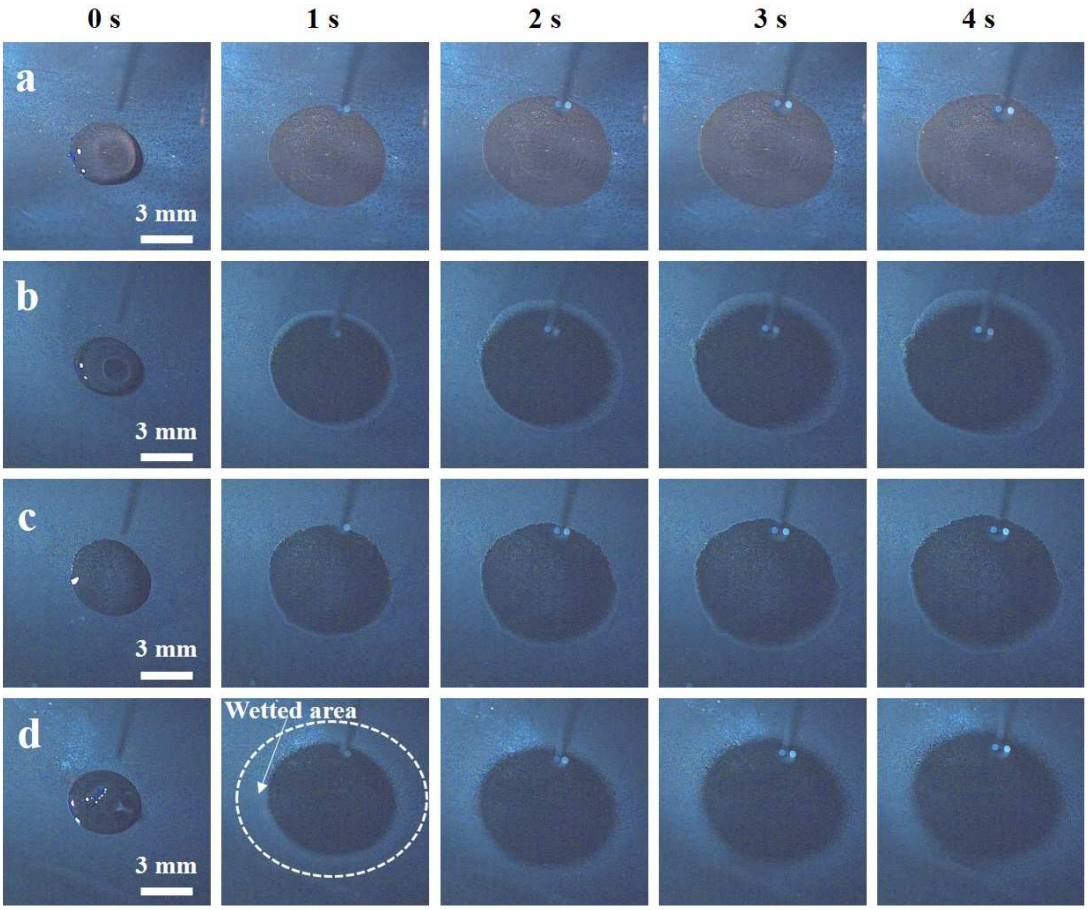

Figure 15. Droplet dynamic behavior analysis (a) NG, (b) NGMP, (c) NGMF, (d) NSMF.

According to the above-mentioned droplet spreading behavior images, the wicking coefficient which can represent the wicking capability of the surface was calculated according to the equation (1). **Figure 16** shows the wicking coefficient as a function of the square root of time on the NG, NGMP, NGMF and NSMF surfaces in the initial 0.5 s. Larger *W* value indicates that the droplet spreads faster and the wetted area becomes larger on the structured surfaces. In obvious, a good linear fit between the wicking coefficient and the wicking distance can be observed. The wicking coefficient of the NG, NGMP, NGMF and NSMF is 1.5, 1.7, 2.1 and 3.8 mm/s$^{0.5}$.

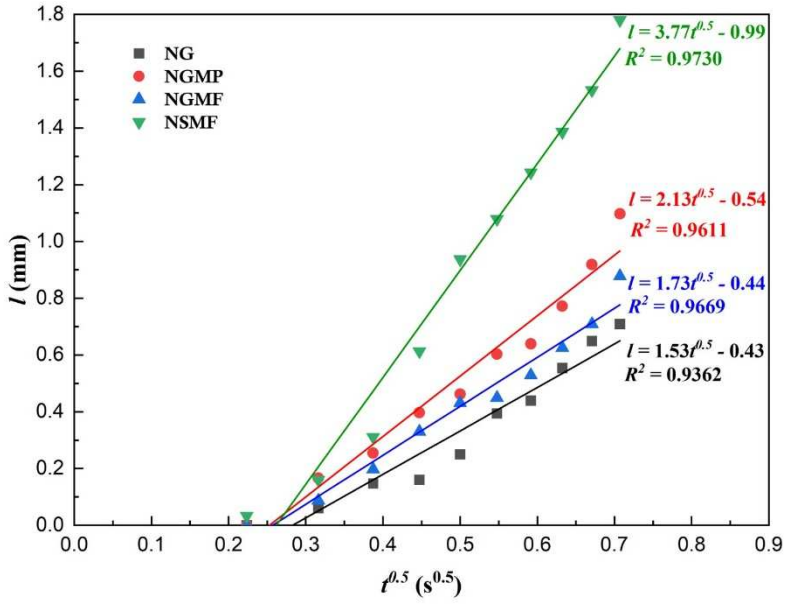

Figure 16. Wicking distance with square root time

To further explore the effect of the oxide presence on the surfaces' wicking capability, we conducted the EDS analysis on the NG, NGMP, NGMF and NSMF surfaces. As shown in **Figure 17a**, **b**, **c**, and **d**, the O content of the NG, NGMP, NGMF and NSMF is 32.5%, 24.9%, 24.7%, 24.3%, respectively. Meanwhile, the Cu content of the NG, NGMP, NGMF and NSMF is 35.5%, 58.3%, 58.6%, 61.3%, respectively. With the increase in the reaction time, the O content decreases and the Cu content increases, indicating that more Cu^{2+} will produce with the presence of O. According to the reaction process as follows [78]:

$$Cu + 2OH^{-1} + S_2O_8^{2-} \rightarrow Cu(OH)_2 + 2SO_4^{2-} \quad (15)$$

$$Cu(OH)_2 \rightarrow CuO + H_2O \quad (16)$$

When the reaction time is shorter, NG surface still has more Na and S contents, indicating that OH^- and $S_2O_8^{2-}$ are not fully participating in the reaction. Thus, the O and Cu contents are smaller on the NG surface. Further increasing the reaction time, more O content can participate in the reaction, and the $Cu(OH)_2$ on the NG converts into the CuO. The O and Cu contents can maintain almost unchanged when the NG structure converts into the other hierarchical structures. This is attributed to the fact that more Cu^{2+} will produce with the presence of more O. When converting into the CuO, the NGMP, NGMF and NSMF become more stable, resulting in no significant formation of the Cu^{2+}. Nevertheless, different wicking performance can be observed on the NG, NGMP, NGMF and NSMF surfaces. Therefore, the presence of oxide has almost no effect on the wicking.

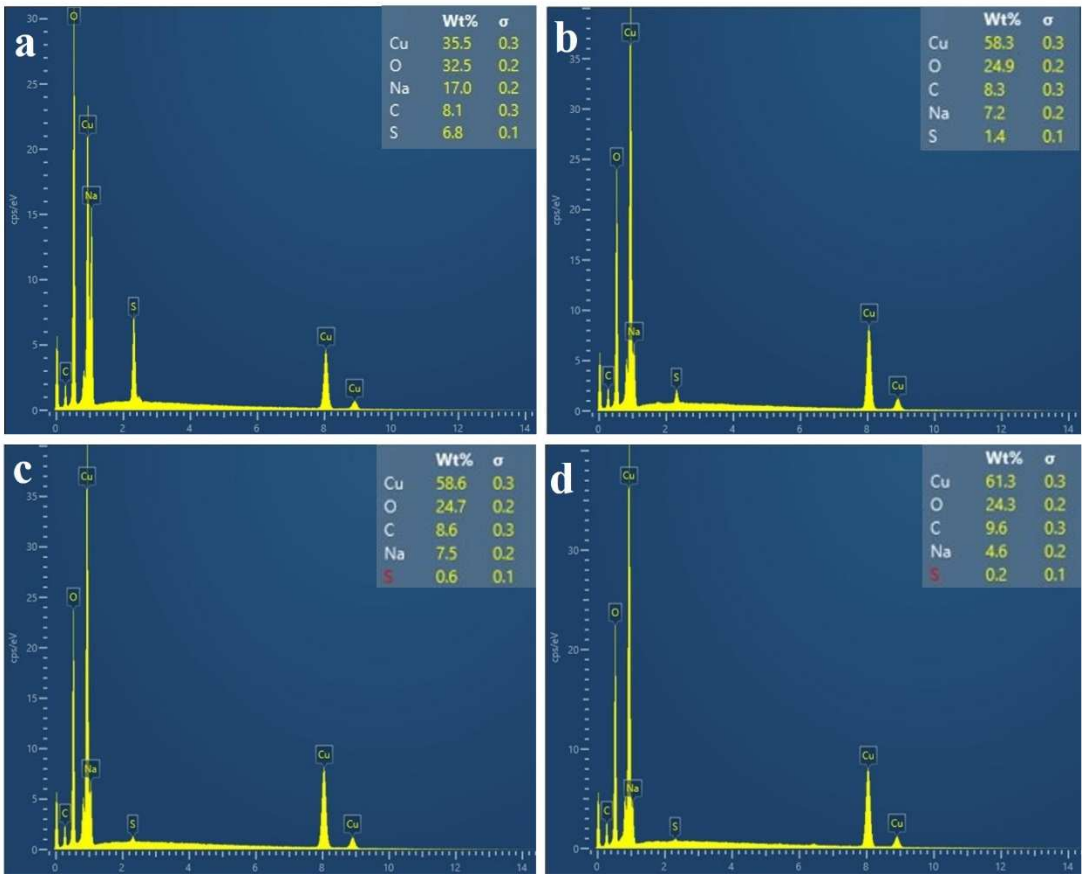

Figure 17. EDS analysis (a) NG, (b) NGMP, (c) NGMF, (d) NSMF

Figure 18 shows the relationships between the CHF and *W*. The wicking coefficient *W* is zero on the smooth surface because of no micro/nanostructures fabricated on its surface. The CHF and wicking coefficient have a linear relationship, which suggests that the *W* alone determines the CHF on the NG, NGMP, NGMF and NSMF. In obvious, the CHF of the NG surface is a little higher than that of the smooth surface. This may be attributed to two factors. First, the $Cu(OH)_2$ on the NG surface is easily to decomposed into the stable CuO [79], which may destroy the nanograss structure on the NG surface. Second, the thickness of $Cu(OH)_2$ nanograss on the NG is very thin (0.9 μm), which will be destroyed during the pool boiling process, resulting in exposing smooth copper surface directly and deteriorating the CHF. Comparing with the NG structures, the hierarchical structures including (NGMP, NGMF and NSMF) have the significantly high CHF. This is attributed to the fact that the NGMP, NGMF and NSMF structures have the higher wicking capability and multilevel roughness [55]. As the wicking coefficient increases, the CHF of NGMF, NGMP and NSMF structure increases, which shows that the CHF augmentation might be caused by a wicking surface with improved wicking capabilities. After the growth of micro/nanocrystals on the smooth surface, the microcavities can be fabricated on the surface for bubble nucleation. Additionally, capillary-driven constant liquid replenishment to the dry-out region can improve the CHF. As a result, the NSMF's largest liquid capillary wicking

capability produces the highest CHF.

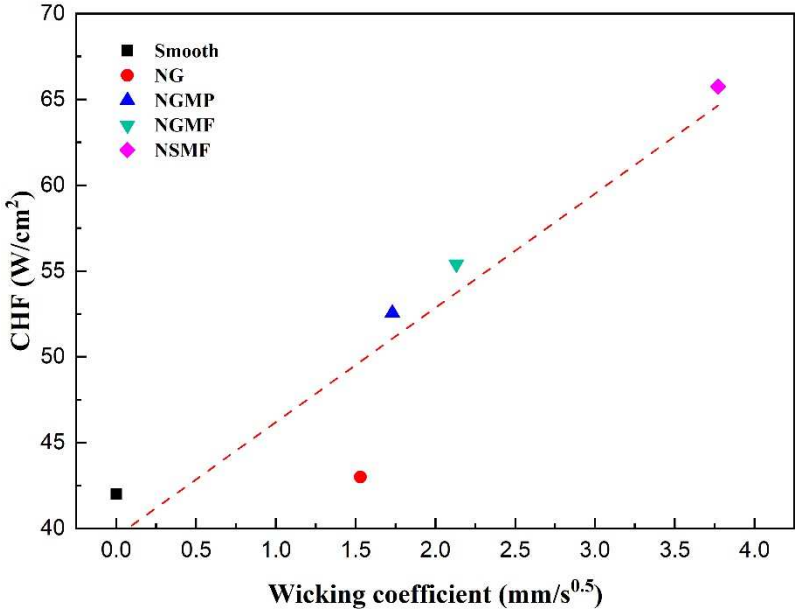

Figure 18. Relationship between CHF and wicking coefficient *W*

3.7 Pool boiling enhancement mechanism

In the nucleate boiling process, the convective heat transfer can be predicted by the bubble departure diameter D_d, nucleation site density N_a and bubble departure frequency f. The equation can be expressed as follows [80]:

$$HTC = 2\sqrt{\pi k_l \sigma C_p}\sqrt{f}\, D_d^2 N_a \tag{17}$$

where k_l, C_p, and σ are the liquid thermal conductivity, specific heat and surface tension, respectively. As aforementioned, the minimum cavity radius required for activation is determined by

$$R_c = \frac{2\sigma T_{sat}}{\rho_l h_{fg} \Delta T} \tag{18}$$

NSMF can provide the suitable size range (5 ~ 15 μm) to act as the cavity for bubble nucleation according to **Figure 4d**. In addition, the cavity radius will become smaller as the wall superheat increases at higher heat flux. Here note that a wall superheat of 5 K refers to a cavity diameter of 13 μm, while a higher wall superheat of 20 K decreases the cavity diameter of 3 μm, which is almost the pore size of the NSMF. Therefore, at the low heat flux, more bubbles can be activated, and the nucleation site density can be significantly increased, resulting in the reduced ONB and the increase in the HTC. As shown in **Figure 19**, with the increase in the heat flux, more micro pores as nucleation sites are activated, small nucleated bubbles in the cavities can absorb heat from the surrounding wall (micro-flower structures) of the cavities, resulting in the faster bubble

growth rate. In addition, the surrounding wall (micro-flower structures) can limit the bubble expansion, accelerating the bubble departure and improving the bubble departure frequency.

At the high heat flux, liquid supply performance which is determined by the capillary pressure significantly affect the pool boiling performance. The capillary pressure can be expressed as follows:

$$\Delta P = 4\sigma / D_P \tag{19}$$

where σ is the surface tension and D_P is the pore size. It is clear that smaller pores can facilitate the liquid to rewet the nucleation, delaying the formation of hot spots and enhancing the CHF. However, the performance of vapor escape is also the other important factor to influence pool boiling performance. The vapor mass rate can be defined as follows [81]:

$$m = \frac{\pi}{12}\left(\frac{\rho_v \sigma}{\mu_v}\right)\left(\frac{\varepsilon D_P^3}{\delta}\right) \tag{20}$$

where ρ_v, μ_v, ε and δ is the vapor density, vapor viscosity, porosity and thickness. According to the equation (20), larger pores can facilitate the vapor mass rate, resulting in better vapor escape. Therefore, according to the above-mentioned equations (19) and (20), the optimized pore size can simultaneously enhance the liquid supply and the vapor escape. As shown in **Figure 19**, the NSMF structure is composed of nanosheet bottom layer and micro-flower top layer. Micro pores can also act as the vapor escape channel to facilitate the bubble departure. Meanwhile, the liquid supply can rewet the cavities (micro pores) immediately through the surrounding wall with small pores, and fast liquid supply can also facilitate the bubble departure. Furthermore, the surrounding wall can prevent the bubble coalescence when bubbles generated from the adjacent micro pores become large enough to some extent. On the bottom, nanosheet structure with thin thickness can serve as the wicking layer to drive the liquid to rewet to the nucleation sites for delaying the formation of hot spots, resulting in the CHF enhancement.

Hence, at the low heat flux, the NSMF structure can provide more nucleation sites for reduced ONB and facilitate bubble departure for improved HTC, while NSMF structure can also facilitate the vapor escape and improve liquid supply at the high heat flux. The integration of the micro pore, micro-flower and nanosheet structures contributes to the better boiling performance comparing with the other structures including NG, NGMP and NGMF.

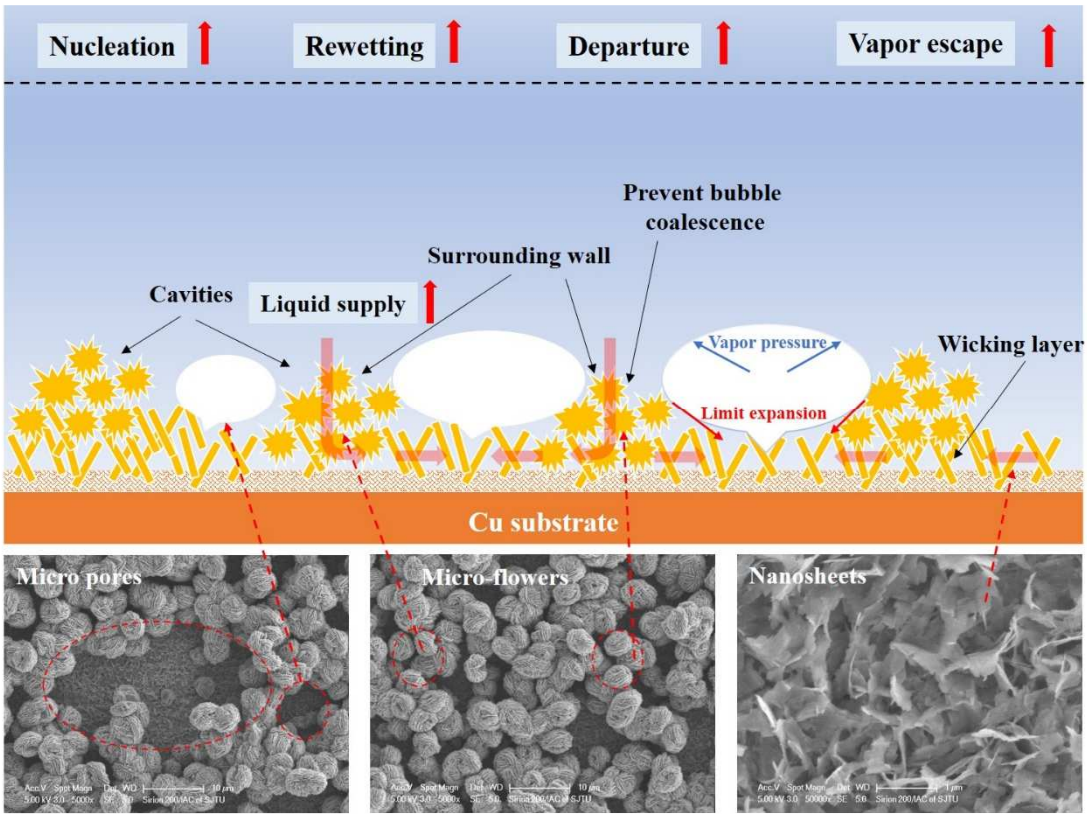

Figure 19. Enhancement mechanism of boiling heat transfer on the NSMF.

4. Conclusions

In this study, the enhancement in pool boiling heat transfer of the hierarchical micro/nanocrystal structures on the Cu substrate in DI water was specifically examined under a wide range of heat fluxes. Based on the experiments, the following conclusions can be drawn:

(1) The SEM, XRD, AFM and XPS methods were used to characterize the morphology and investigate the chemical content of these hierarchical micro/nanocrystals. With the in-situ growth on the Cu substrate, the nanoneedles (NG), nanoneedles and micro-petals (NGMP), nanoneedles and micro-flowers (NGMF) and nanosheets, nanosheets and micro-flowers (NSMF) can be synthesized. The thickness of the NG, NGMP, NGMF and NSMF are 0.9, 4.7, 4.9 and 5.0 μm, respectively. The compositions of the NG, NGMP, NGMF and NSMF are $Cu(OH)_2$ and CuO according to the XRD analysis.

(2) Compared with the capillary wicking on the NG, NGMP, NGMF and NSMF surfaces, the NSMF surface has the largest capillary wicking number W_i of 0.3, which is higher than those values on the NG, NGMP and NGMF surfaces. The experiments indicate that the surface roughness and morphology are responsible for the improvements in capillary wicking.

(3) Compared with the smooth and hierarchical structures, NSMF surface has the

largest CHF of 65.7 W/cm^2, which implies a significant improvement of 56.5%, 55.8%, 18.6% and 25.1% compared to the smooth surface, the NG, NGMP, and NGMF, respectively. Meanwhile, the HTC can be augmented to 4.9 W/cm^{2}K on the NSMF surface, which is larger than that of other surfaces in the same conditions. Moreover, superheat for the ONB on the NSMF is only 5.1^{o}C, which is 43.3%, 26.1%, 17.7% and 25.0% lower than those on the smooth surface, the NG, NGMP, NGMF, respectively.

(4) These significant improvements are due to the enhanced capillary wicking and increased bubble releasing frequency in the boiling phenomenon caused by the special hierarchical morphology of the NSMF surface. As a result, the dynamics by the liquid circulation is remarkably strengthened while the resistance by the coalescence of bubbles and formation of vapor film is largely reduced. Nonetheless, the surface wettability and the measurement accuracy of the experimental apparatus are also pivotal factors that need to be optimized. Further experimental investigations are to be completed towards a breakthrough of the heat transfer performance on such hierarchical structures.

Acknowledgements

This research is financially supported by National Key Research and Development Program (No.2022YFE0198800), and National Natural Science Foundation of China (No. 52076139).

References

[1] S. Xie, M. Shahmohammadi Beni, J. Cai, J. Zhao, Review of critical-heat-flux enhancement methods, International Journal of Heat and Mass Transfer, 122 (2018) 275-289.

[2] X. Ma, J. Xu, J. Xie, In-situ phase separation to improve phase change heat transfer performance, Energy, 230 (2021).

[3] X. Li, S. Wang, R. Wen, X. Ma, R. Yang, Liquid film boiling enabled ultra-high conductance and high flux heat spreaders, Cell Reports Physical Science, 3 (2022).

[4] B.S. Kim, S. Shin, D. Lee, G. Choi, H. Lee, K.M. Kim, H.H. Cho, Stable and uniform heat dissipation by nucleate-catalytic nanowires for boiling heat transfer, International Journal of Heat and Mass Transfer, 70 (2014) 23-32.

[5] Z. Cao, Z. Ouyang, Z. Liu, Y. Li, Y. Ouyang, J. Lin, X. Xie, J. Long, Effects of surface oxides and nanostructures on the spontaneous wettability transition of laser-textured copper surfaces, Applied Surface Science, 560 (2021).

[6] H. Kim, D.E. Kim, Effects of surface wettability on pool boiling process: Dynamic and thermal behaviors of dry spots and relevant critical heat flux triggering mechanism, International Journal of Heat and Mass Transfer, 180 (2021).

[7] B. Shen, T. Hamazaki, W. Ma, N. Iwata, S. Hidaka, A. Takahara, K. Takahashi, Y. Takata, Enhanced pool boiling of ethanol on wettability-patterned surfaces, Applied Thermal Engineering, 149 (2019) 325-331.

[8] H. Hu, Y. Zhao, Z. Lai, C. Hu, Influence of surface wettability on pool boiling heat transfer on metal foam covers, International Journal of Thermal Sciences, 168 (2021).
[9] X.Z. Sun, Q. Li, W.X. Li, Z.X. Wen, B. Liu, Enhanced pool boiling on microstructured surfaces with spatially-controlled mixed wettability, International Journal of Heat and Mass Transfer, 183 (2022).
[10] G. Liang, Y. Chen, J. Wang, Z. Wang, S. Shen, Experiments and modeling of boiling heat transfer on hybrid-wettability surfaces, International Journal of Multiphase Flow, 144 (2021).
[11] B.J. Zhang, K.J. Kim, H. Yoon, Enhanced heat transfer performance of alumina sponge-like nano-porous structures through surface wettability control in nucleate pool boiling, International Journal of Heat and Mass Transfer, 55 (2012) 7487-7498.
[12] H.S. Jo, M.-W. Kim, K. Kim, S. An, Y.I. Kim, S.C. James, J. Choi, S.S. Yoon, Effects of capillarity on pool boiling using nano-textured surfaces through electrosprayed BiVO4 nano-pillars, Chemical Engineering Science, 171 (2017) 360-367.
[13] B.J. Zhang, K.J. Kim, Nucleate pool boiling heat transfer augmentation on hydrophobic self-assembly mono-layered alumina nano-porous surfaces, International Journal of Heat and Mass Transfer, 73 (2014) 551-561.
[14] C. Young Lee, M.M. Hossain Bhuiya, K.J. Kim, Pool boiling heat transfer with nano-porous surface, International Journal of Heat and Mass Transfer, 53 (2010) 4274-4279.
[15] S. Li, R. Furberg, M.S. Toprak, B. Palm, M. Muhammed, Nature-Inspired Boiling Enhancement by Novel Nanostructured Macroporous Surfaces, Advanced Functional Materials, 18 (2008) 2215-2220.
[16] D. Lee, B.S. Kim, H. Moon, N. Lee, S. Shin, H.H. Cho, Enhanced boiling heat transfer on nanowire-forested surfaces under subcooling conditions, International Journal of Heat and Mass Transfer, 120 (2018) 1020-1030.
[17] H.S. Jo, T.G. Kim, J.-G. Lee, M.-W. Kim, H.G. Park, S.C. James, J. Choi, S.S. Yoon, Supersonically sprayed nanotextured surfaces with silver nanowires for enhanced pool boiling, International Journal of Heat and Mass Transfer, 123 (2018) 397-406.
[18] H. Zhao, S. Dash, N.S. Dhillon, S. Kim, B. Lettiere, K.K. Varanasi, A.J. Hart, Microstructured Ceramic-Coated Carbon Nanotube Surfaces for High Heat Flux Pool Boiling, ACS Applied Nano Materials, 2 (2019) 5538-5545.
[19] K. Lu, X. Wei, F. Xue, M. Liu, Semiconductor nanotubes enhance boiling heat transfer, International Journal of Heat and Mass Transfer, 164 (2021).
[20] G. Udaya Kumar, K. Soni, S. Suresh, K. Ghosh, M.R. Thansekhar, P. Dinesh Babu, Modified surfaces using seamless graphene/carbon nanotubes based nanostructures for enhancing pool boiling heat transfer, Experimental Thermal and Fluid Science, 96 (2018) 493-506.
[21] P. Dančová, R. Kaniowski, R. Pastuszko, Comparison of heat transfer coefficients of open micro-channels and plain micro-fins, EPJ Web of Conferences, 180 (2018).
[22] J. Long, Z. Liu, H. Lin, Y. Li, Z. Cao, Z. Zhang, X. Xie, Pool boiling heat transfer and bubble dynamics over V-shaped microchannels and micropyramids: Does high aspect ratio always benefit boiling?, Applied Thermal Engineering, 201 (2022).
[23] H.J. Kwak, J.H. Kim, B.-S. Myung, M.H. Kim, D.E. Kim, Behavior of pool boiling heat transfer and critical heat flux on high aspect-ratio microchannels, International Journal of Thermal Sciences, 125 (2018) 111-120.
[24] H. Tang, L. Xia, Y. Tang, C. Weng, Z. Hu, X. Wu, Y. Sun, Fabrication and pool boiling performance assessment of microgroove array surfaces with secondary micro-structures for high power applications,

Renewable Energy, 187 (2022) 790-800.
[25] J. Zhou, B. Qi, J. Wei, Critical heat flux on heterogeneous fractal surfaces with micro-pin-fins in pool boiling Part I: The effects of distribution and subcooling, International Journal of Heat and Mass Transfer, 136 (2019) 1338-1348.
[26] B. Liu, X. Yang, Z. Jie, J. Wei, Q. Li, Enhanced pool boiling on micro-nano composited surfaces with nanostructures on micro-pin-fins, International Journal of Heat and Mass Transfer, 190 (2022).
[27] Y. Zhang, X. Ma, Z. Zhu, L. Duan, J. Wei, Critical heat flux prediction model of pool boiling heat transfer on the micro-pillar surfaces, Case Studies in Thermal Engineering, 28 (2021).
[28] K.-H. Chu, R. Enright, E.N. Wang, Structured surfaces for enhanced pool boiling heat transfer, Applied Physics Letters, 100 (2012).
[29] H.W. Moon, Y.J. Yoon, J.H. Park, B.-S. Myung, D.E. Kim, Dynamic wetting and boiling characteristics on micro-structured and micro/nano hierarchically structured surfaces, Experimental Thermal and Fluid Science, 74 (2016) 19-26.
[30] S.H. Kim, G.C. Lee, J.Y. Kang, K. Moriyama, M.H. Kim, H.S. Park, Boiling heat transfer and critical heat flux evaluation of the pool boiling on micro structured surface, International Journal of Heat and Mass Transfer, 91 (2015) 1140-1147.
[31] S. Jun, J. Kim, D. Son, H.Y. Kim, S.M. You, Enhancement of Pool Boiling Heat Transfer in Water Using Sintered Copper Microporous Coatings, Nuclear Engineering and Technology, 48 (2016) 932-940.
[32] C.M. Patil, K.S.V. Santhanam, S.G. Kandlikar, Development of a two-step electrodeposition process for enhancing pool boiling, International Journal of Heat and Mass Transfer, 79 (2014) 989-1001.
[33] H. Liu, C. Zhang, J. Wang, L. Zhang, Critical heat flux enhancement using composite porous structure produced by selective laser melting, Applied Thermal Engineering, 197 (2021).
[34] W. Zhou, X. Hu, L. Mao, Y. He, Markedly enhanced pool boiling heat transfer performance on maicropaorous copper surfaces fabricated utilizing a facile wire cutting process, Applied Thermal Engineering, 165 (2020).
[35] J. Shi, X. Jia, D. Feng, Z. Chen, C. Dang, Wettability effect on pool boiling heat transfer using a multiscale copper foam surface, International Journal of Heat and Mass Transfer, 146 (2020).
[36] S.A. Khan, N. Sezer, M. Koç, Design, fabrication and nucleate pool-boiling heat transfer performance of hybrid micro-nano scale 2-D modulated porous surfaces, Applied Thermal Engineering, 153 (2019) 168-180.
[37] A. Mehdikhani, H. Moghadasi, H. Saffari, An experimental investigation of pool boiling augmentation using four-step electrodeposited micro/nanostructured porous surface in distilled water, International Journal of Mechanical Sciences, 187 (2020).
[38] D. Kong, M. Kang, K.Y. Kim, J. Jang, J. Cho, J.B. In, H. Lee, Hierarchically Structured Laser-Induced Graphene for Enhanced Boiling on Flexible Substrates, ACS Appl Mater Interfaces, 12 (2020) 37784-37792.
[39] C.H. Li, T. Li, P. Hodgins, C.N. Hunter, A.A. Voevodin, J.G. Jones, G.P. Peterson, Comparison study of liquid replenishing impacts on critical heat flux and heat transfer coefficient of nucleate pool boiling on multiscale modulated porous structures, International Journal of Heat and Mass Transfer, 54 (2011) 3146-3155.
[40] A. Jaikumar, S.G. Kandlikar, Enhanced pool boiling heat transfer mechanisms for selectively sintered open microchannels, International Journal of Heat and Mass Transfer, 88 (2015) 652-661.
[41] G. Chen, C.H. Li, Combined effects of liquid wicking and hydrodynamic instability on pool boiling

critical heat flux by two-tier copper structures of nanowires and microgrooves, International Journal of Heat and Mass Transfer, 129 (2019) 1222-1231.
[42] D. Lee, N. Lee, D.I. Shim, B.S. Kim, H.H. Cho, Enhancing thermal stability and uniformity in boiling heat transfer using micro-nano hybrid surfaces (MNHS), Applied Thermal Engineering, 130 (2018) 710-721.
[43] Z. Yao, Y.W. Lu, S.G. Kandlikar, Pool Boiling Heat Transfer Enhancement Through Nanostructures on Silicon Microchannels, Journal of Nanotechnology in Engineering and Medicine, 3 (2012).
[44] C.M. Patil, S.G. Kandlikar, Pool boiling enhancement through microporous coatings selectively electrodeposited on fin tops of open microchannels, International Journal of Heat and Mass Transfer, 79 (2014) 816-828.
[45] G. Chen, N. Chukwunenye, G.F. Jones, C.H. Li, Biomimetic Structures by Leaf Vein Growth Mechanism for Pool Boiling Heat Transfer Enhancements, International Journal of Heat and Mass Transfer, 155 (2020).
[46] P. Xu, Q. Li, Y. Xuan, Enhanced boiling heat transfer on composite porous surface, International Journal of Heat and Mass Transfer, 80 (2015) 107-114.
[47] Y.-Q. Wang, S.-S. Lyu, J.-L. Luo, Z.-Y. Luo, Y.-X. Fu, Y. Heng, J.-H. Zhang, D.-C. Mo, Copper vertical micro dendrite fin arrays and their superior boiling heat transfer capability, Applied Surface Science, 422 (2017) 388-393.
[48] J. Li, W. Fu, B. Zhang, G. Zhu, N. Miljkovic, Ultrascalable Three-Tier Hierarchical Nanoengineered Surfaces for Optimized Boiling, ACS Nano, 13 (2019) 14080-14093.
[49] R. Wen, Q. Li, W. Wang, B. Latour, C.H. Li, C. Li, Y.-C. Lee, R. Yang, Enhanced bubble nucleation and liquid rewetting for highly efficient boiling heat transfer on two-level hierarchical surfaces with patterned copper nanowire arrays, Nano Energy, 38 (2017) 59-65.
[50] J. Kim, S. Jun, J. Lee, J. Godinez, S.M. You, Effect of Surface Roughness on Pool Boiling Heat Transfer of Water on a Superhydrophilic Aluminum Surface, Journal of Heat Transfer, 139 (2017).
[51] J.C. Godinez, D. Fadda, J. Lee, S.M. You, Development of a stable Boehmite layer on aluminum surfaces for improved pool boiling heat transfer in water, Applied Thermal Engineering, 156 (2019) 541-549.
[52] Y. Im, C. Dietz, S.S. Lee, Y. Joshi, Flower-Like CuO Nanostructures for Enhanced Boiling, Nanoscale and Microscale Thermophysical Engineering, 16 (2012) 145-153.
[53] S. Xie, M. Jiang, H. Kong, Q. Tong, J. Zhao, An experimental investigation on the pool boiling of multi-orientated hierarchical structured surfaces, International Journal of Heat and Mass Transfer, 164 (2021).
[54] S. Xie, X. Ma, H. Kong, S. Bai, M. Jiang, J. Zhao, The synergetic effects of the surface wettability and the patterned nanostructure on boiling heat transfer enhancement, International Journal of Heat and Mass Transfer, 176 (2021).
[55] J. Li, Y. Zhao, J. Ma, W. Fu, X. Yan, K.F. Rabbi, N. Miljkovic, Superior Antidegeneration Hierarchical Nanoengineered Wicking Surfaces for Boiling Enhancement, Advanced Functional Materials, 32 (2021).
[56] D.I. Shim, G. Choi, N. Lee, T. Kim, B.S. Kim, H.H. Cho, Enhancement of Pool Boiling Heat Transfer Using Aligned Silicon Nanowire Arrays, ACS Appl Mater Interfaces, 9 (2017) 17595-17602.
[57] P. De Jaeger, C. T'Joen, H. Huisseune, B. Ameel, S. De Schampheleire, M. De Paepe, Assessing the influence of four bonding methods on the thermal contact resistance of open-cell aluminum foam,

International Journal of Heat and Mass Transfer, 55 (2012) 6200-6210.
[58] L.L. Manetti, G. Ribatski, R.R. de Souza, E.M. Cardoso, Pool boiling heat transfer of HFE-7100 on metal foams, Experimental Thermal and Fluid Science, 113 (2020).
[59] C. Gerardi, J. Buongiorno, L.-w. Hu, T. McKrell, Study of bubble growth in water pool boiling through synchronized, infrared thermometry and high-speed video, International Journal of Heat and Mass Transfer, 53 (2010) 4185-4192.
[60] N. Zuber, Hydrodynamic ASDects of Boiling Heat Transfer, Atomic Energy Commission Report, (1959).
[61] J. Linehard, V.K. Dhir, Extended hydrodynamic theory of the peak and minimum pool boiling heat fluxes, NASA Contractor Reports, (1973).
[62] S.G. Kandlikar, A Theoretical Model to Predict Pool Boiling CHF Incorporating Effects of Contact Angle and Orientation, Journal of Heat Transfer, 123 (2001) 1071-1079.
[63] H.H. Son, S.J. Kim, Role of receding capillary flow correlating nano/micro scale surface roughness and wettability with pool boiling critical heat flux, International Journal of Heat and Mass Transfer, 138 (2019) 985-1001.
[64] T.J. Hendricks, S. Krishnan, C. Choi, C.-H. Chang, B. Paul, Enhancement of pool-boiling heat transfer using nanostructured surfaces on aluminum and copper, International Journal of Heat and Mass Transfer, 53 (2010) 3357-3365.
[65] H. Zhao, C.P. Garner, Corrections for the Hydrodynamic Instability-Based Critical Heat Flux Models in Pool Boiling—Effects of Viscosity and Heating Surface Size, Journal of Heat Transfer, 140 (2018).
[66] H.H. Son, G.H. Seo, U. Jeong, D.Y. Shin, S.J. Kim, Capillary wicking effect of a Cr-sputtered superhydrophilic surface on enhancement of pool boiling critical heat flux, International Journal of Heat and Mass Transfer, 113 (2017) 115-128.
[67] C.S. Sujith Kumar, Y.W. Chang, P.-H. Chen, Effect of heterogeneous wettable structures on pool boiling performance of cylindrical copper surfaces, Applied Thermal Engineering, 127 (2017) 1184-1193.
[68] Z. Yao, Y.W. Lu, S.G. Kandlikar, Effects of nanowire height on pool boiling performance of water on silicon chips, International Journal of Thermal Sciences, 50 (2011) 2084-2090.
[69] A. Amiri, M. Shanbedi, H. Amiri, S.Z. Heris, S.N. Kazi, B.T. Chew, H. Eshghi, Pool boiling heat transfer of CNT/water nanofluids, Applied Thermal Engineering, 71 (2014) 450-459.
[70] J. Han Kim, A. Gurung, M. Amaya, S. Muk Kwark, S.M. You, Microporous Coatings to Maximize Pool Boiling Heat Transfer of Saturated R-123 and Water, Journal of Heat Transfer, 137 (2015).
[71] M.-C. Lu, R. Chen, V. Srinivasan, V.P. Carey, A. Majumdar, Critical heat flux of pool boiling on Si nanowire array-coated surfaces, International Journal of Heat and Mass Transfer, 54 (2011) 5359-5367.
[72] X. Cheng, G. Yang, J. Wu, Spontaneously grown boehmite structures improve pool boiling heat transfer on aluminium surfaces, International Journal of Heat and Mass Transfer, 192 (2022).
[73] D.-C. Mo, S. Yang, J.-L. Luo, Y.-Q. Wang, S.-S. Lyu, Enhanced pool boiling performance of a porous honeycomb copper surface with radial diameter gradient, International Journal of Heat and Mass Transfer, 157 (2020).
[74] M.M. Rahman, M. McCarthy, Boiling Enhancement on Nanostructured Surfaces with Engineered Variations in Wettability and Thermal Conductivity, Heat Transfer Engineering, 38 (2016) 1285-1295.
[75] W. Zhou, L. Mao, X. Hu, Y. He, An optimized graphene oxide self-assembly surface for significantly enhanced boiling heat transfer, Carbon, 150 (2019) 168-178.

[76] Y. Liu, M.-C. Lu, D. Xu, The suppression effect of easy-to-activate nucleation sites on the critical heat flux in pool boiling, International Journal of Thermal Sciences, 129 (2018) 231-237.
[77] I. Malenkov, Detachment frequency as a function of size for vapor bubbles, Journal of Engineering Physics, 20 (1971) 704-708.
[78] J. Li, X. Liu, Y. Ye, H. Zhou, J. Chen, Fabrication of Superhydrophobic CuO Surfaces with Tunable Water Adhesion, The Journal of Physical Chemistry C, 115 (2011) 4726-4729.
[79] J. Feng, Z. Qin, S. Yao, Factors affecting the spontaneous motion of condensate drops on superhydrophobic copper surfaces, Langmuir, 28 (2012) 6067-6075.
[80] A.R. Betz, J. Jenkins, C.-J.C. Kim, D. Attinger, Boiling heat transfer on superhydrophilic, superhydrophobic, and superbiphilic surfaces, International Journal of Heat and Mass Transfer, 57 (2013) 733-741.
[81] E. Meléndez, R. Reyes, The pool boiling heat transfer enhancement from experiments with binary mixtures and porous heating covers, Experimental Thermal and Fluid Science, 30 (2006) 185-192.